A cytomegalovirus immunevasin triggers integrated stress response-dependent reorganization of the endoplasmic reticulum.

Running Title: HCMV UL148 reorganizes the ER.

Hongbo Zhang[a,1], Clarissa Read[d,e,1], Christopher C. Nguyen[a] , Mohammed N.A. Siddiquey[a], Chaowei Shang[c], Cameron M. Hall[a], Jens von Einem[d], and Jeremy P. Kamil[a,b #]

[a]Department of Microbiology and Immunology,
[b]Center for Molecular and Tumor Virology
[c]Research Core Facility
LSU Health Sciences Center, Shreveport, Louisiana, USA

[d] Institute of Virology, Ulm University Medical Center,
[e]Central Facility for Electron Microscopy, Ulm University
Ulm, Germany
[1] these authors contributed equally to the study

Running Head: HCMV UL148 Remodels the ER

#Address correspondence to Jeremy P. Kamil, jkamil@lsuhsc.edu

ABSTRACT. Human cytomegalovirus (HCMV) encodes an ER-resident glycoprotein, UL148, which activates the unfolded protein response (UPR) but is fully dispensable for viral replication in cultured cells. Hence, its previously ascribed roles in immune evasion and modulation of viral cell tropism are hypothesized to cause ER stress. Here, we show that UL148 is necessary and sufficient to drive the formation of large ER-derived structures that occupy up to 7% of the infected cell cytosol. The structures are found to be sites where UL148 coalesces with cellular proteins involved in ER quality control, such as Hrd1 and EDEM1. Transmission electron microscopy analyses reveal the structures to be comprised of tortuous, densely packed and apparently collapsed ER membranes that connect to distended cisternae. During induced ectopic expression of UL148-GFP fusion protein, punctate signals traffic to accumulate at prominent structures that exhibit poor recovery of fluorescence after photobleaching. Small molecule blockade of the integrated stress response (ISR) prevents the formation of puncta, leading to a uniform reticular fluorescent signal. Accordingly, ISR inhibition during HCMV infection abolishes the coalescence of UL148 and Hrd1 into discrete structures, which argues that UL148 requires the ISR to cause ER reorganization. Given that UL148 stabilizes immature forms of a receptor binding subunit for a viral envelope glycoprotein complex important for HCMV infectivity, our results imply that stress-dependent ER remodeling contributes to viral cell tropism.

IMPORTANCE.

Perturbations to ER morphology occur during infection with various intracellular pathogens and in certain genetic disorders. We identify that an HCMV gene product, UL148, profoundly reorganizes the ER during infection, and is sufficient to do so when expressed on its own. Our results reveal that UL148-dependent reorganization of the ER is a

49 prominent feature of HCMV infected cells. Moreover, we find that this example of virally
50 induced organelle remodeling requires the integrated stress response (ISR), a stress
51 adaptation pathway that contributes to a number of disease states. Since ER
52 reorganization accompanies the roles of UL148 in HCMV cell tropism and intracellular
53 retention of the immune cell co-stimulatory ligand CD58, our results may have implications
54 for understanding the mechanisms involved. Furthermore, our findings provide a basis to
55 utilize UL148 as a tool to investigate organelle responses to stress and to identify novel
56 drugs targeting the ISR.
57
58 **INTRODUCTION.**
59 UL148 is a human cytomegalovirus (HCMV) ER-resident glycoprotein that plays
60 roles in evasion of cell-mediated immunity and shows intriguing effects on cell tropism.
61 During infection of epithelial cells, viruses disrupted for *UL148* replicate to produce roughly
62 100-fold enhanced levels of infectious progeny virions compared to wildtype (1). These
63 effects correlate with reduced expression of glycoprotein O (gO), a subunit of a
64 heterotrimeric viral glycoprotein H (gH) / glycoprotein L (gL) complex (gH/gL/gO) that is
65 required for the infectivity of cell-free virions (2-4). The presence of gO in the context of the
66 heterotrimer endows the virus with the capacity to utilize the platelet derived growth factor
67 receptor α (PDGFRα) as an entry receptor (5-7). Accordingly, UL148 has been found to
68 stabilize immature forms of gO prior their assembly into gH/gL/gO heterotrimers (1, 8).
69 Despite that UL148 does not stably associate with gO, the data suggest an interaction with
70 gH (1).
71 UL148 also physically associates with CD58 (LFA-3), a co-stimulatory ligand for
72 natural killer cells and T-lymphocytes, preventing its presentation at cell surface (9).
73 Although the mechanisms by which UL148 stabilizes gO and retains CD58 within the ER

74 remain unknown, UL148 strongly contributes to activation of the unfolded protein response
75 (UPR) during infection, and is sufficient to activate the UPR when ectopically expressed in
76 non-infected cells (10). UL148 co-purifies from infected cells with SEL1L, an adaptor
77 subunit of ER-based E3 ubiquitin ligase Hrd1 that plays important roles in ER-associated
78 degradation (ERAD) of terminally misfolded glycoproteins (8). This suggests a physical
79 interaction with ERAD machinery, which may be germane to the mechanism by which
80 UL148 activates the UPR.

81 Here, we show that the expression of UL148 is necessary and sufficient to induce
82 unusual ER structures at which large quantities of ER factors involved in glycoprotein
83 quality control accumulate. In electron microscopy analyses, we find that the UL148
84 induced ER-structures are comprised of densely packed, tortuous ER membranes that form
85 connections with tubules of highly distended cisternal space. Furthermore, additional data
86 from inhibitor studies strongly argue that ER remodeling triggered by UL148 requires the
87 integrated stress response. Overall, our results reveal a striking ER perturbation induced
88 by HCMV, and which is entirely controlled by a single viral gene product. These findings
89 may have important implications for understanding how UL148 regulates viral cell tropism
90 and/or contributes to viral evasion of cell-mediated immunity.
91

92 **RESULTS.**

93

94 **UL148 causes reorganization of ER quality control proteins into unusual globular**
95 **structures.**

96 The HCMV ER-resident glycoprotein UL148 was previously observed to co-localize
97 with the ER marker calnexin during infection (1). Nonetheless, calnexin staining did not
98 show the uniform reticular pattern characteristic for the ER marker. We later noticed that
99 cells infected with a *UL148*-null virus showed uniform calnexin staining (see below). To
100 formally determine whether UL148 influences calnexin localization, we compared
101 fibroblasts at four days post-infection with either wildtype strain TB40/E virus (TB_WT) or a
102 *UL148*-null mutant (TB_148$_{STOP}$)(8, 10), each derived from an infectious bacterial artificial
103 chromosome (BAC) clone of HCMV strain TB40/E (11) (**FIG 1**). In cells infected with
104 wildtype virus, calnexin antibodies stained unusual globular structures at the cell periphery,
105 as expected (1) (**FIG 1A, 1C, SI FIG S1A**). However, in cells infected with the *UL148*-null
106 virus, calnexin staining was uniform throughout the cytosol (**FIG 1B-C**), as would be
107 expected for an ER marker in uninfected cells. The staining pattern for Hrd1, another ER
108 marker, likewise indicated accumulation at unusual globular structures during wildtype
109 HCMV infection, but not during infection with *UL148*-null mutant viruses (**FIG 1, S1A**).
110 Because calnexin and Hrd1 staining showed uniform distribution in *UL148*-null virus
111 infected cells, and because *UL148* is fully dispensable for efficient viral replication in
112 fibroblasts (1), these results suggest that redistribution of these two ER markers depends
113 on UL148.

114 As expected (12, 13), antibodies specific for glycoprotein H (gH), a viral envelope
115 glycoprotein, stained a juxtanuclear compartment, termed the cytoplasmic virion assembly
116 compartment (cVAC), which does not involve the ER (**FIG 1**). Similarly contrasting staining

117 patterns for Hrd1 and/or calnexin were observed in cells infected with wildtype versus
118 *UL148*-null mutants of clinical HCMV strains Merlin and TR (**FIG S1**). Reciprocally, we
119 restored a functional *UL148* at its native locus in the context of a BAC clone of HCMV strain
120 AD169, which spontaneously lost most of the gene in the course of extensive genetic
121 rearrangements that occurred during serial passage in cultured cells. In cells infected with
122 AD169 repaired for UL148, but not the *UL148*-null parental virus, the Hrd1 staining pattern
123 showed prominent globular structures (**FIG S1**).

124 Because similar differences in Hrd1 staining are observed between wildtype and
125 *UL148*-null infections of THP-1 macrophages, ARPE-19 epithelial cells and fibroblasts (**FIG**
126 **1, FIG S1**), we concluded that UL148-dependent reorganization of ER markers occurs in
127 multiple cell types. The calnexin staining pattern seen with four different primary clinical
128 isolates from patient throat swabs likewise indicated punctate globular structures. These
129 observations, taken together with results from formal comparisons of wildtype versus
130 *UL148*-null mutants of four different BAC-cloned HCMV strains (**FIG 1, FIG S1**), argue that
131 UL148 profoundly affects the ER during natural infection.

132 We measured the three-dimensional volume of UL148-dependent Hrd1 structures
133 from sixteen cells fixed at 96 h post infection (hpi) with strain TB40/E. On average, the
134 structures occupied 303.3 μm^3 (SEM: +/- 24.8) out of a total cell volume of 7657 μm^3
135 (SEM:+/- 651.0), which was estimated using a phalloidin-fluorophore conjugate to detect
136 the actin cytoskeleton (**FIG 1D-E**). Subtracting the volume of nuclei, as indicated by 4′,6-
137 diamidino-2-phenylindole [DAPI] (average nucleus: 1360 μm^3, SEM:+/-129.4), we calculate
138 that, on average, the structures occupy 5.2% of the cytosolic volume (SEM: +/-0.61%,
139 range: 2.0% – 7.0%). Based on these findings, taken together with results comparing
140 additional wildtype (WT) versus *UL148*-null mutant HCMV strains (**FIG S1**), we conclude
141 that the UL148-dependent ER structures are a prominent feature of HCMV-infected cells.

142 UL148 substantially contributes to activation of the unfolded protein response (UPR)
143 during HCMV infection (10), and co-purifies from infected cells with SEL1L (8), an adaptor
144 subunit for the E3 ubiquitin ligase Hrd1, which plays crucial roles in ER-associated
145 degradation (ERAD) of terminally misfolded glycoprotein substrates (14). Hence, the
146 accumulation of Hrd1 and calnexin at unusual structures during wildtype but not *UL148*-null
147 infection may suggest that structures form in response to defects in ER quality control
148 (ERQC) caused by UL148. Under conditions of proteasome inhibition, overexpression of
149 certain misfolded glycoproteins causes cellular factors involved in ERQC, such as calnexin,
150 to compartmentalize from the rest of the ER, while other ER markers such as BiP (Grp78)
151 or protein disulfide isomerase (PDI) remain largely unaltered (15-17).
152 To gain further insights into the nature of these peculiar ER structures, we set out to
153 develop a more comprehensive understanding of their protein composition by comparing
154 the localization of selected ER markers at 96 hpi during infection with either TB_148^{HA} (1),
155 a recombinant HCMV strain TB40/E virus that expresses UL148 fused at its C-terminus to
156 the nonapeptide epitope tag YPYDVPDYA from influenza A hemagglutinin (HA), or
157 TB_159^{HA}, a *UL148*-null comparator in which the UL148 homolog from rhesus
158 cytomegalovirus, *Rh159*, likewise fused to a C-terminal HA tag, is expressed in lieu of
159 UL148.
160 We considered the TB_159^{HA} virus to be an appropriate control for the following
161 reasons. Firstly, Rh159 and UL148 exhibit ~30% identity at the amino acid level and both
162 glycoproteins localize to the ER and block cell surface presentation immune cell activating
163 ligands; UL148 retains CD58, a ligand for CD2, while Rh159 retains NKG2D ligands of the
164 MIC- and ULBP families (1, 9, 18). Secondly, Rh159 is expressed from TB_159^{HA} at
165 comparable levels and with similar kinetics observed for UL148 from TB_148^{HA}, and the
166 two viruses replicate indistinguishably in fibroblasts (**FIG 2**). Moreover, as was the case in

167 ectopic expression (10), Rh159 does not appear to activate the UPR to the same extent
168 that UL148 does, as evidenced by lower levels of phospho-eIF2α and ATF4 during
169 TB_159^{HA} infection (**FIG 2A**).
170 ERQC markers failed to coalesce into unusual structures during infection with
171 TB_159^{HA} (**FIG 3**). The structures likewise failed to occur in rhesus fibroblasts during
172 infection with a recombinant rhesus cytomegalovirus (RhCMV) that we engineered to
173 express an HA-tag fused at the C-terminus of Rh159 (**FIG S1**). The latter argues against
174 the possibility that Rh159 somehow requires the context of rhesus cells to redistribute ER
175 markers in a manner analogous to what is seen for UL148 during HCMV infection. Taken
176 together, the data suggest that UL148 and Rh159 authentically differ in their effects on the
177 secretory pathway.
178 In cells infected with TB_148^{HA}, HA antibody staining indicated localization of UL148
179 to globular structures, as expected (1). Antibody signals from indirect confocal
180 immunofluorescence detection of cellular ER resident proteins involved in ERQC, including
181 calnexin, Hrd1, SEL1L, Herp, valosin containing protein (VCP, p97), and EDEM1, strongly
182 co-localized with signals from HA-tagged UL148 (**FIG 3-4**). These results indicate that a
183 number of ERQC factors coalesce with UL148 to form prominent globular structures in
184 infected cells. In contrast, we observed uniform ER staining patterns for PDI and
185 calreticulin (CALR), indicating that these ER markers do not localize to the UL148
186 structures (**FIG 3Q, 3S**). Intriguingly, antibody signals detecting reticulon 3 and ribophorin
187 1, which are markers for smooth ER and rough ER, respectively, each appreciably co-
188 localized with UL148 (HA) signal at the induced structures (**FIG 3K, 3M)**, which indicates
189 that the structures may involve both rough and smooth ER. LC3B failed to co-localize with
190 the structures (**FIG S2**), as might be expected given that the virus inhibits macroautophagy

191 at late times during infection (19, 20). Nevertheless, our results suggested that the induced
192 structures are enriched for a related mammalian ATG8 ortholog, GABARAP (**FIG 3O**).
193 In cells infected with TB_159^{HA}, all of the ER markers we examined showed uniform,
194 reticular staining, as did the anti-HA signal detecting Rh159 (**FIG 3B, D, F, H, J, L, N, R, T,**
195 **V**). EDEM1, in addition to showing reticular staining, also labeled puncta associated with
196 the nucleus (**FIG 3J, 3I**), which may represent enriched levels of the protein at the rough
197 ER membranes associated with the nuclear envelope, although we cannot exclude the
198 possibility of spurious intranuclear staining. GABARAP antibodies stained the cVAC in
199 TB_159^{HA} infected cells, but also showed a much weaker diffuse signal throughout the
200 cytosol. Even though we took steps to block viral Fc receptors, which can cause rabbit
201 antibodies to non-specifically label the cVAC (21), it is plausible that GABARAP antibody
202 signal from the cVAC reflects incomplete blocking of viral Fc receptors. For both viruses,
203 antibodies specific for the TGN marker syntaxin-6 (STX6) and gH, as expected, stained the
204 juxtanuclear cVAC structure (12, 13, 22), a post-ER compartment that excludes UL148 (1)
205 (**FIG S2**).
206 To quantify the degree of co-localization with UL148, we calculated Pearson's
207 correlation coefficients from a minimum of thirty TB_148^{HA} infected cells per staining
208 condition (fixation at 4 dpi), comparing the signal overlap for each ER marker to the HA
209 signal from UL148. The correlation coefficients (*r*) for staining patterns from antibodies
210 specific for EDEM1, Hrd1, reticulon-3 (RTN3), SEL1L, the ER retention motif KDEL, and
211 calnexin ranged from 0.8 to 0.72. These results suggest that these proteins, and lumenal
212 ER resident proteins such as BiP (GRP78) and GRP94 that contain a C-terminal KDEL
213 motif (EKDEL), extensively co-localize with UL148 at the induced structures (**FIG 4**).
214 Meanwhile, GABARAP, VCP, ribophorin-1 (RPN1), and Herp showed *r* values in the range
215 of 0.54 to 0.51, indicating a moderate degree of co-localization with UL148. However,

216 CALR and PDI, which like BiP, are lumenal ER residents, and the TGN marker syntaxin-6,
217 gave *r* values of close to zero, indicating that these markers do not appreciably co-localize
218 with UL148, as is consistent with our immunofluorescence data suggesting that these
219 markers negligibly associate with the unusual structures. From these results, we conclude
220 that the UL148-dependent ER structures are enriched for cellular markers involved in
221 glycoprotein quality control. In this regard, the structures resemble the "ER quality control
222 (ERQC) compartments" described by G. Lederkremer and colleagues (15, 16, 23). We
223 further conclude that Rh159 cannot substitute for UL148 to redistribute ERQC markers.
224

225 **VCP and Hrd1 are recruited to incipient UL148 ER structures prior to calnexin.**

226 To determine whether there might be differences in the kinetics of recruitment of
227 ERQC markers during formation of the ER structures, we examined a series of time points
228 from one to four days post-infection (dpi) with wildtype HCMV strain TB40/E carrying HA-
229 tagged UL148, staining for three different ERQC markers, calnexin, Hrd1, and VCP,
230 alongside UL148 (HA). At 1 dpi the signal from UL148 was only faintly detected, as
231 expected (1), while each of the ER markers was readily detected, providing a readout of
232 their staining patterns prior to being substantially perturbed by UL148 (**FIG S3**). At 2 dpi,
233 we detected robust anti-HA signal, indicating the presence of UL148. At this time point,
234 UL148 exhibited intense signal at small globular puncta, which we interpret to represent
235 incipient UL148 structures, as well as more diffuse staining of a reticular structure
236 consistent with undisturbed ER. Calnexin did not appreciably co-localize with the UL148
237 puncta until at least 3 dpi, and the structures were not readily visualized by calnexin
238 staining until 4 dpi (**FIG S3**). In contrast, signals from Hrd1 and VCP staining were sufficient
239 to mark the UL148 puncta by 2 dpi, which suggests that these markers may co-localize with
240 UL148 at earlier points during the genesis of the ER structures. Notably, the appearance of

241 Hrd1 at the structures prior to calnexin is consistent with our previous results showing that
242 UL148 co-purifies from infected cells with SEL1L, an adaptor subunit for Hrd1 (8). These
243 results imply that basal elements of the ERAD machinery, exemplified by Hrd1 and VCP,
244 might be recruited to UL148-induced ER structures prior to calnexin.
245
246 **Visualization of UL148-induced ER structures by electron microscopy.**
247 To discern the ultrastructural appearance of the UL148 structures and to formally ascertain
248 their relationship to the ER, we carried out transmission electron microscopy (TEM)
249 imaging of wildtype (TB_WT) and *UL148*-null (TB_148$_{STOP}$) infected fibroblasts at 5 dpi. In
250 high pressure frozen and freeze-substituted infected fibroblasts, cells with a high density of
251 viral nucleocapsids within the nucleus were selected for analysis, as this feature indicates
252 late time points during infection when UL148 is abundantly expressed. The TEM results
253 revealed prominent globular and oblong structures in the cytoplasm of wildtype virus
254 infected fibroblasts, but not *UL148*-null infected controls (**FIG 5-6**). The structures stand out
255 for their high electron-density, which may reflect the abundance of ERQC proteins together
256 with UL148 in these structures. Under higher magnification, these areas are characterized
257 by accumulations of densely packed ruffled membranes and membranous material, which
258 appear to either be collapsed ER, or ER tubules in very close association with each other.
259 The membrane accumulations were associated with smooth and partially rough ER
260 structures of seemingly enlarged cisternal space. Further, tomographic reconstruction of
261 scanning transmission electron microscopy (STEM) data suggest that densely packed ER
262 cisternae within the structures are interconnected and continuous in three-dimensional
263 space (**FIG 7B-C, Movie S1**).
264
265 **UL148 accumulates in a detergent-insoluble form during infection.**

266 Disease-associated variants of certain cellular proteins, such as the A103E mutant
267 of the calcium channel Orai1, and the E342K "Z" variant of alpha-1 antitrypsin (Z A1AT),
268 localize to anomalous ER structures reminiscent of those we observe to depend on UL148
269 (17, 24-27). A103E Orai1 and Z A1AT are found to accumulate in detergent-insoluble
270 forms within the ER or within ER membranes, respectively, which indicates aggregation or
271 polymerization of these proteins, and suggests a mechanism for the formation of ER
272 structures by the proteins (17, 24, 27, 28). We therefore set out to determine whether
273 differences in solubility might correlate with the differing potentials UL148 and Rh159 to
274 cause ER reorganization and to activate the UPR (10). To address this question, we
275 infected fibroblasts with TB_148^{HA} or TB_159^{HA} at MOI 1 and at various times post-
276 infection prepared cell lysates in radioimmunoprecipitation assay (RIPA) buffer. After
277 subjecting the lysates to high-speed centrifugation, we examined the relative levels of
278 UL148 and Rh159 in the detergent-soluble supernatant and detergent-insoluble pellet
279 fractions.
280 A substantial portion of UL148 was detected from the detergent-insoluble fractions at
281 all time points tested (**FIG 8**). Furthermore, the percentage of UL148 detected within the
282 insoluble fraction increased over time. In contrast, Rh159 was found only in the detergent-
283 soluble fraction. From these results, we conclude that UL148 accumulates in a detergent-
284 insoluble form during infection, and that Rh159 does not do so. Because the anti-HA
285 immunoreactive band detected in both the soluble and insoluble fractions from TB_148^{HA}
286 infected cells showed a relative mobility of ~35 kD, which matched that expected for the
287 mature, endoH-sensitive glycoprotein (1), these findings argue that UL148 may form
288 aggregates or polymers within the ER.
289
290 **UL148 is sufficient to compartmentalize the ER.**

291 Our data thus far demonstrate that UL148 is necessary during infection to cause
292 redistribution of cellular ER markers for glycoprotein quality control processes, such that
293 substantial portion of the ERQC machinery appears to become sequestered away from the
294 rest of the organelle into novel membranous structures. Because a number of viral proteins
295 that remodel the ER during infection are sufficient to alter ER morphology when ectopically
296 expressed [e.g. (29),(30), reviewed in (31)], we wondered whether UL148 expression would
297 be sufficient to induce ER structures akin to those seen during HCMV infection. Making
298 use of "tet-on" ARPE-19 epithelial cells that inducibly express either UL148 or Rh159, each
299 carrying a C-terminal HA-tag (32), we induced transgene expression for 48 h and
300 subsequently stained for various cellular markers for the ER, for ERQC as well as for the
301 ATG8 family proteins LC3B and GABARAP, which play roles in macroautophagy and
302 related processes.

303 In cells expressing UL148 (i148^{HA}), we observed that calnexin, Hrd1, EDEM1, and
304 VCP co-localized with UL148 at prominent globular structures reminiscent of those
305 observed during infection (**FIG S4**). The respective rough and smooth ER markers
306 ribophorin 1 (RPN1) and reticulon 3 (RTN3), as well as the ATG8 proteins LC3B and
307 GABARAP likewise co-localized to the UL148-induced structures. However, PDI and CALR
308 each failed to substantially co-localize with UL148 at the structures (**FIG S4**), or at best
309 showed only limited co-localization, consistent with our results from infected cells (**FIG 3-4**).
310 Signals from antibodies specific for the KDEL (EKDEL) motif important for ER retrieval of
311 luminal ER residents, such as BiP and GRP94, likewise showed only limited co-localization
312 with UL148. The PDI and KDEL results suggest that large regions of the ER are not
313 involved in the UL148 structures.

314 In cells expressing the UL148 homolog Rh159 (i159^{HA}), we detected uniform
315 cytoplasmic distribution of ER markers, as well as of HA-tagged Rh159, similar to what we

316 observed during infection with the recombinant HCMV TB_159^{HA} (**FIG 3**). Furthermore, in
317 this setting the staining patterns for the ATG8 family proteins LC3B and GABARAP failed to
318 indicate any notable structures. Consistent with our previous study showing that UL148, but
319 not Rh159, is sufficient to activate the UPR (10), we observed accumulation of ATF4 and
320 phosphorylated eIF2α following doxycycline (dox) induced expression of UL148 but not
321 Rh159 (**FIG 9A**). Importantly, the intensity of HA signals detecting UL148 and Rh159
322 indicated that both ER resident immunevasins accumulate at roughly comparable levels
323 following dox induction. This argues against the possibility that gross protein expression
324 differences accounts for the differing effects of UL148 and Rh159 on UPR activation and on
325 the staining patterns for ER markers.

326 Pearson's correlation coefficient values were calculated to quantify the extent of
327 colocalization between UL148 and various cellular markers: EDEM1, Hrd1, VCP, calnexin
328 (CNX), RTN3, SEL1L, LC3B, and PDI (**FIG 9B**). The results quantitatively buttress the
329 confocal immunofluorescence results from these cells (**FIG S4**). We therefore conclude
330 that no other HCMV gene products are required for UL148 to cause ERQC factors to
331 segregate into discrete compartments. Hence, we conclude from these findings that UL148
332 is sufficient to cause large-scale reorganization of ERQC markers. Moreover, these results
333 suggest that reorganization of ER markers into discrete structures may be related to the
334 propensity of UL148 to induce ER stress.

335 To determine whether UL148-dependent ER remodeling could be visualized in real-
336 time using live cell imaging, we constructed new "tet-on" lentiviral vectors that inducibly
337 express either UL148 or Rh159 fused at their predicted C-terminal cytoplasmic tails to the
338 enhanced green fluorescent protein (GFP) from *Aequorea victoria* (33). Following lentiviral
339 transduction, we isolated puromycin-resistant ARPE-19 and subsequently subjected to
340 fluorescence-activated cell sorting (FACS) to enrich for cells that expressed GFP signal

341 following dox treatment. The resulting cell populations, which inducibly express either
342 UL148-GFP or Rh159-GFP, were designated i148^{GFP} and i159^{GFP}, respectively.
343 In live cell imaging studies, we observed that the GFP signal in dox-induced i148^{GFP}
344 cells first appeared in a reticular, largely uniform pattern, which was readily visible at 5 h
345 post-induction. However, by 9 h post-induction punctate signals began to appear. These
346 puncta were observed to traffic to sites of large-scale accumulation, where large
347 fluorescent structures progressively increased in size up until the termination of the
348 experiment at 19 h (**FIG S5, Movie S2**). In contrast, i159^{GFP} cells exhibited a largely
349 diffuse, reticular GFP signal at all time points monitored subsequent to transgene induction
350 (**FIG S5, Movie S3**). The live cell imaging results thus recapitulated the differences in the
351 HA-staining patterns observed between dox-induced i148^{HA} and i159^{HA} cells following
352 fixation, as well as those between HCMV expressing HA-tagged UL148 versus *UL148*-null
353 comparator viruses (**FIG 1, 3, Fig S1**).
354
355 **UL148-GFP structures exhibit poor recovery of fluorescence after photobleaching.**
356 To determine whether the protein contents of the UL148 induced structures exhibits
357 decreased mobility compared to non-perturbed ER regions, we carried out fluorescence
358 recovery after photobleaching (FRAP) studies. We photobleached regions of GFP signal in
359 i148^{GFP} or i159^{GFP} ARPE-19 cells that had been induced for transgene expression for 24 h,
360 and then monitored recovery of fluorescence over a 5 min time period. In Rh159-GFP
361 expressing cells (i159^{GFP}), fluorescence nearly recovered to pre-bleach levels within 3 min,
362 and by 5 min fully recovered (**FIG S6**). In contrast, when we photobleached a prominent
363 UL148-GFP structure, the GFP signal failed to appreciably recover fluorescence during the
364 same 5 min time period. Nonetheless, regions of reticular GFP signal from an i148^{GFP} cell,
365 which presumably represent ER regions not involved in an anomalous structure, recovered

366 fluorescent signal with kinetics similar to those observed during Rh159-GFP expression.
367 These results indicate that bleached UL148-GFP within the structures cannot rapidly be
368 exchanged with UL148-GFP from other portions of the organelle, which suggests that the
369 induced UL148 structures do not exchange their contents as efficiently as unperturbed ER.
370

371 **Ectopically-expressed UL148 is degraded by proteasomes and not by autophagy.**

372 The UL148 ER structures were found to be enriched with proteins such as Hrd1,
373 SEL1L, EDEM, and VCP (**FIG 3-4**, **9B, FIG S4**), which are posited to play key roles in
374 ERAD, a process during which misfolded glycoproteins are recognized, processed, and
375 dislocated across the ER membrane for degradation at cytosolic proteasomes. However,
376 we also detected elements of the machinery for autophagy in close association with the
377 UL148 structures. Namely, the mammalian ATG8 ortholog GABARAP co-localized with
378 UL148 during infection (**FIG 3-4**), and both GABARAP and another ATG8 ortholog, LC3B,
379 co-localized with UL148 at the ER structures during ectopic expression of UL148 (**FIG 9B,**
380 **FIG S4**). Therefore, we wished to determine whether UL148 is degraded by the
381 proteasome, as would be consistent with conventional ERAD, or by the lysosome, which
382 would suggest a role for autophagy-related processes, such as selective autophagy of the
383 ER (34), in dispensing with UL148, and presumably, in resolving the ER perturbations.

384 As a first step, we conducted a live-cell imaging "washout" experiment in which
385 i148^{GFP} cells were induced for transgene expression for 24 h, after which the growth
386 medium containing the transgene inducing agent (dox) was replaced with medium lacking
387 dox. During a 22 h imaging period following dox-washout, we observed the structures to
388 become progressively smaller as the reticular and punctate GFP signals gradually abated
389 (**SI FIG S7, Movie S7**). Because the results suggested that UL148-GFP structures could
390 be resolved over time, we induced UL148-GFP in tet-on ARPE-19 cells (i148^{gfp}) for 24 h,

391 washed out the inducing agent (dox), and then applied either epoxomicin (20 μM), an
392 irreversible inhibitor of the proteasome (35), or folimycin (115 nM), a proton pump inhibitor
393 that blocks autophagosome maturation and impedes lysosome-dependent degradation (36,
394 37). Of the two inhibitors, only epoxomicin stabilized UL148 (**SI FIG S7**). Although
395 folimycin treatment had no obvious effect on UL148-GFP levels, the drug markedly
396 increased the levels of LC3B-II, as would be expected with the lysosomal proton pump
397 inhibitor. From these results, we conclude that ectopically expressed UL148 is primarily
398 degraded by proteasome-dependent pathway.
399
400 **UL148 requires the integrated stress response to cause ER reorganization.**
401 We previously reported that UL148 triggers the UPR during ectopic expression, and
402 that UL148 contributes to activation of the PKR-like ER kinase (PERK) and inositol
403 requiring enzyme 1 (IRE1) during infection (10). The literature suggests that formation of
404 ERQC compartments requires PERK (38). PERK responds to ER stress by activating the
405 integrated stress response (ISR). In particular, PERK phosphorylates eIF2α at Ser51, and
406 the accumulation of phosphorylated eIF2α (eIF2α-P) globally attenuates mRNA translation
407 whilst stimulating the translation of a subset of mRNAs, such as those encoding ATF4 and
408 CHOP, which play roles in cellular adaptation to stress (39). Stress-regulated translation of
409 such mRNAs involves small upstream open reading frames (uORFs) in their 5' untranslated
410 regions that ordinarily suppress translation under basal conditions (40, 41).
411 To examine whether ER remodeling in response to UL148 requires the ISR, we
412 turned to a well characterized small molecule inhibitor of stress-regulated translation, ISRIB
413 (42-46). ISRIB is thought to act as a "molecular staple" that holds the guanine nucleotide
414 exchange factor eIF2B in an active decameric configuration (44-47), such that eIF2B will
415 continue to generate ternary complex (eIF2•GTP•Met-tRNAi) necessary for new cycles of

416 translational initiation, despite the presence of eIF2α-P. Because PERK is the kinase that
417 phosphorylates eIF2α in response to ER stress (48, 49), we also tested for effects of the
418 PERK inhibitor GSK2606414 (50). Having confirmed that ISRIB and GSK260641 do not
419 negatively impact UL148 expression during dox-induction of UL148-GFP **(FIG 10)**, we
420 treated i148^{GFP} cells with 200 nM ISRIB, 1.1 μM GSK260641, or DMSO vehicle control, and
421 carried out live cell imaging during induction of UL148-GFP expression.
422 ISRIB and GSK6060414 virtually abolished the formation of UL148 puncta through
423 13 h post induction (dox addition), a time point at which the DMSO control condition
424 showed abundant large structures (**FIG 10C-E, SI Movies S8-S10**). Based on our findings
425 (**FIG 1, 3, 5, 7, 9B, S4)**, we interpret the formation and subsequent large-scale aggregation
426 of UL148-GFP puncta to faithfully indicate ER reorganization in response to UL148.
427 Therefore, these results suggested to us that pharmacological inhibition of either the ISR or
428 PERK prevent UL148 from remodeling the ER, which implies that ER remodeling in
429 response to ER stress requires stress-regulated translation.
430 Since our results with ISRIB and GSK6060414 indicated that the ISR is required for
431 ER remodeling to occur during ectopic expression of UL148, we next asked whether these
432 pharmacological agents would prevent UL148-dependent ER remodeling in the
433 physiologically authentic context of HCMV infection. Our live cell imaging studies from
434 ISRIB and GSK6060414 treatments indicated that UL148-GFP puncta could begin to
435 appear by ~19 h post treatment (**FIG 10, SI Movies S9-S10**), which suggested that the
436 pharmacological activity of the drugs might diminish over time. Thus to ensure that
437 blockade of PERK and the ISR would be sustained over the 4 d period that it takes for
438 structures to fully form during HCMV infection, we replenished drug treatments every 24 h,
439 replacing the spent media with media containing freshly reconstituted ISRIB, GSK6060414,
440 or DMSO vehicle control.

441 At 4 dpi, ER structures were readily visible in DMSO control treatment condition but
442 virtually abolished in the ISRIB and GSK2606414 conditions (**FIG 11A**). To quantify these
443 effects, we obtained Z-stacks from a minimum of 30 cells per treatment condition and used
444 Imaris 3D image analysis software to calculate the percentage of Hrd1 signal that
445 coalesced into discrete structures during infection. The results indicated highly significant
446 differences between the DMSO carrier alone setting compared to treatments with either
447 GSK2606414 or ISRIB (**FIG 11B**). In the DMSO control condition, on average, 10% of the
448 Hrd1 signal was found to be associated with the UL148 structures (arithmetic mean; range
449 5.8% – 17.6%), as indicated by structures delimited by HA signal detecting UL148. In the
450 presence of ISRIB or GSK2606414, however, these values were reduced to 2.8% (range:
451 0.69% – 7.1%) and 3.6% (range: 0.8%-6.5%), respectively. Reassuringly, roughly
452 equivalent levels of UL148 were detected in Western blot analyses of protein extracts from
453 drug treated and DMSO control conditions. Therefore, differences in UL148 expression are
454 unlikely to explain the observed failure of UL148 and Hrd1 to coalesce into ER structures
455 during inhibition of either the ISR or PERK. Meanwhile, ISRIB and GSK2606414
456 treatments both led to reduced levels of ATF4 accumulation, while the PERK inhibitor alone
457 was able to reduce the levels eIF2α-P, as indicated by a phospho-specific antibody.
458 Therefore, each of the drugs caused the expected effects on the PERK, eIF2α-P, and
459 ATF4 axis (**FIG 11C-D**).
460 A modest reduction in the levels of the viral envelope glycoprotein B (gB) was
461 observed during treatments with ISRIB or GSK2606414. This may suggest that the ISR is
462 required for optimal expression of the certain viral envelope glycoproteins. Even though
463 UL148 promotes ATF4 expression, likely via PERK activation (10), viruses that lack *UL148*
464 cause high levels of ATF4 accumulation at late times during infection, which is when viral
465 late gene products, such a gB, are expressed at their highest levels (10). Hence, the

466 activity of PERK and/or of the ISR may be required for optimal expression of viral envelope
467 glycoproteins. Regardless, the PERK inhibitor and ISRIB each prevented the appearance
468 of discrete UL148 ER structures while failing to substantially affect UL148 expression.
469 Therefore, the effects of the two inhibitors on UL148-dependent ER reorganization were
470 consistent with those seen during ectopic expression of the protein. Taken together, our
471 findings argue that the ISR is required for UL148 to cause remodeling of the organelle.

472 **DISCUSSION**

473 The ER structures that we have identified are noteworthy in several regards. Firstly,
474 this example of virally-induced ER remodeling is wholly dependent on a single viral gene
475 product, UL148. Of course, there are other examples of individual viral gene products that
476 are necessary to grossly perturb ER morphology during infection which are also found to be
477 sufficient to induce such perturbations [e.g., (29, 30, 51, 52)]. Nonetheless, the ER
478 structures caused by UL148 are— to the best of our knowledge, a hitherto undescribed
479 ultrastructural characteristic of the HCMV infected cell, which is surprising given their size,
480 scale, and prominence. Indeed, the average volume of the structures at 96 h postinfection
481 amounts to roughly 60% of the size of the nucleus of an uninfected human fibroblast [~500
482 μm^3, (53)]. Although UL148 expression is accompanied by UPR activation, ER
483 reorganization occurs without killing the host cell, even in the setting of ectopic expression
484 when viral functions that inhibit programmed cell death are absent. Nor does UL148 affect
485 the yield of infectious virus during replication in fibroblasts, since *UL148*-null mutant viruses
486 replicate indistinguishably from wildtype parental virus in this cell type (1, 8). As with all
487 enveloped viruses, HCMV requires the host cell secretory pathway to fold and process
488 enormous quantities of viral envelope glycoproteins that endow progeny virions with the
489 molecular machinery for infectivity. It is intriguing to consider how the infected cell tolerates
490 spatial reorganization of ER membranes and of the associated glycoprotein quality control
491 machinery without impacting the production of infectious progeny virions.

492 Furthermore, certain aspects of ER reorganization invoked by UL148 may be novel
493 to cell biology. In particular, the densely packed collapsed ER in close association with
494 varicosities that we observe to depend on UL148 during infection appear to differ from the
495 ER structures induced by other ER perturbagens. For instance, a hereditary form of
496 childhood cirrhosis caused by the *Z* allele of the alpha-1-antitrypsin (Z-A1AT) gene

497 (*SERPINA*) is characterized by polymerization of Z-A1AT within the ER (26), leading to its
498 accumulation in membrane-delimited inclusions (26, 27, 54). However, Z-A1AT inclusions
499 are not observed to associate with regions of collapsed ER, nor does Z-A1AT suffice to
500 activate the UPR, even though its expression sensitizes cells to other triggers of ER stress
501 (27, 55).

502 HCMV encodes at least one other ER-resident immunevasin that activates the UPR,
503 US11 (56). UL148 binds the NK-cell and T-cell costimulatory ligand CD58 to prevent its
504 transport to the cell surface while US11 targets the heavy chain of class I major
505 histocompatibility complex (MHC) for ER-associated degradation (57, 58). UL148 causes
506 CD58 to accumulate as an immature glycoform, presumably within the ER, but does not
507 lead to any obvious decrease in its overall abundance (9). Albeit that intracellular forms of
508 CD58 are in our hands refractory to detection by standard indirect immunofluorescence
509 protocols (data not shown), it seems reasonable to hypothesize that UL148 sequesters
510 CD58 into the unusual ER structures that it induces. Moreover, our detergent solubility
511 results suggest that UL148 may form aggregates or polymers in the course of preventing
512 CD58 presentation at the cell surface (FIG 8). It is worth noting that UL148, an
513 immunevasin targeting CD58, induces dramatic morphologic rearrangements of the ER,
514 while another HCMV immunevasin, US11, targeting MHC class I for degradation evidently
515 does not do so, even though both trigger ER stress. Nonetheless, it seems unlikely that
516 retention of CD58 would be required for ER reorganization. In fact, the capacity of UL148
517 to retain CD58 may be functionally separable from its peculiar effects on the morphology
518 and organization of the ER.

519 Despite that the relationship between the mechanism for CD58 retention and the
520 formation of UL148-dependent ER structures remains unresolved, our findings may
521 suggest a mechanism to explain the influence of UL148 on the tropism of the virus for

522 epithelial cells. These effects, exemplified by a ~100-fold replication advantage of *UL148*-
523 null viruses during infection of epithelial cells, correlate with decreased expression of
524 glycoprotein O (gO), a viral envelope glycoprotein, both in virions and in infected cells (1).
525 We previously reported that gO behaves as a constitutive ERAD substrate during infection
526 and that immature, newly synthesized forms of gO show enhanced stability in the presence
527 of UL148 (8). Our findings herein show that UL148 causes large-scale sequestration of
528 cellular factors important for ERAD, such as the ER mannosidase EDEM1 and the E3
529 ubiquitin ligase SEL1L/Hrd1, into large membranous structures. Moreover, the reticular
530 ER, as indicated by the staining patterns of antibodies specific for calreticulin, PDI, and the
531 KDEL motif, appears to remain largely intact following UL148-induced ER reorganization
532 (FIG 3, 10). Since these observations indicate that UL148 depletes ERAD factors from the
533 ER during the formation of the unusual structures, regions of ER not drawn into the
534 structures might be expected to offer a more permissive folding environment for
535 polypeptides, such as gO, which either fold slowly or inefficiently assemble into multiprotein
536 complexes.

537 Based on these observations, one might hypothesize that UL148 alters ER
538 proteostasis by physically dislocating (or sequestering) key elements of the "mannose
539 removal time clock" system that marks poorly folding glycoproteins for destruction via
540 ERAD (59, 60). Because gO is both the defining subunit of the heterotrimeric gH/gL/gO
541 envelope glycoprotein complex that governs HCMV entry and cell tropism (5-7, 61, 62), and
542 a constitutive ERAD substrate (1, 8), ER reorganization might be required for the effects of
543 UL148 on HCMV cell tropism. Going forward, it will be crucial to determine whether
544 classical ERAD substrates, such as the null Hong Kong variant of alpha-1-antitrypsin (63,
545 64) or ribophorin-332 (65, 66), are stabilized during UL148 expression, as would be
546 predicted if UL148 shifts ER proteostasis to negatively modulate ERAD.

547 In addition to having found that factors involved in proteasomal ERAD, such as Hrd1
548 and EDEM1, are enriched at the UL148 structures, we observed that GABARAP, a
549 mammalian ortholog of yeast ATG8, localizes to the UL148 ER structures during infection,
550 and that another ATG8 ortholog, LC3B, and GABARAP both associate with the structures
551 during ectopic expression of UL148. This may suggest roles for autophagy-related
552 pathways in UL148-dependent reorganization of the organelle. Since our results indicate
553 that UL148 is degraded by a proteasome-dependent pathway and not by lysosomes (**FIG**
554 **S7**), it seems unlikely that selective autophagy of the ER is directly involved in recycling or
555 degrading these ER structures. Nonetheless, ATG8 family proteins may contribute to
556 formation of the globular ER structures, since we observed trafficking of UL148-GFP
557 puncta to form large aggregates during live cell imaging (**FIG 12, 15, Movies S2, S8**). The
558 literature indicates that misfolded proteins traffic in a microtubule (MT)-dependent manner
559 to form pericentriolar structures termed aggresomes, which in the case of ERAD substrates
560 such as the ΔF508 mutant of the cystic fibrosis transmembrane conductance regulator
561 (CFTR), contain deglycosylated protein that presumably has already undergone dislocation
562 from the ER (67, 68). ATG8 family proteins such as LC3B and GABARAP not only play
563 roles in degradation of substrates via macroautophagy, but also bind MTs and recruit
564 machinery for MT-dependent transport of cargos (69-71). Therefore, GABARAP and LC3B
565 may be important for the recruitment of cellular machinery that transports perturbed ER
566 cargoes to sites of large-scale accumulation.
567 Although our results argue that the ISR is required for ER reorganization during
568 UL148 expression, precisely how UL148 triggers ER stress remains unknown. UL148 has
569 been found to co-purify from cells with SEL1L, a component of the ERAD machinery.
570 Thus, it seems plausible that UL148 may inhibit the Hrd1/SEL1L complex, which would
571 cause the buildup of unfolded proteins and thus trigger the UPR. However, inhibition of

572 ERAD in and of itself seems unlikely to account for the formation of ER structures. Another
573 non-mutually exclusive possibility is that UL148 multimerizes or aggregates in a manner
574 that constricts the ER lumen. For instance, the assembly of UL148 molecules on opposite
575 sides of the ER lumen might constrict the organelle in a manner consistent with the
576 collapsed regions of ER observed in our EM results (**FIG 6, 8**).
577 Additional work will be needed to decipher the molecular mechanisms by which
578 UL148 causes reorganization of the ER, and to determine its physiological relevance in the
579 setting of viral biology. Nonetheless, we have shown that UL148, when fused to a
580 fluorescent protein (FP), suffices both to trigger and to indicate the presence of a functional
581 ISR (**FIG 10-11, S5**). Hence, UL148-FP fusions may prove useful in high throughput
582 chemical-genetic screens to identify novel small molecule inhibitors of the ISR as well as to
583 identify cellular genes involved in stress-dependent remodeling of the ER. Interestingly, the
584 two pharmacological agents that block UL148-dependent ER remodeling, ISRIB and
585 GSK2606414, are known to prevent the formation of stress granules (SGs) (43, 72). SGs
586 are comprised of condensed aggregates of protein and RNA which occur due to stalled
587 mRNA translation in the context of disease states, such as amyotrophic lateral sclerosis
588 (73), as well as during treatments with toxic agents such as arsenite (43, 72). It is
589 fascinating to consider that mechanistic parallels exist between the formation of SGs and
590 the UL148-dependent reorganization of the ER. Moreover, given the broad importance
591 macromolecular aggregation in pathological conditions such as neurodegenerative
592 diseases (74), certain of which also involve defects in ER proteostasis and aberrant
593 activation of the UPR, UL148 may hold promise as tool to discover new agents to
594 ameliorate disease.
595

596 **MATERIALS AND METHODS.**

597

598 **Cells and virus.**

599 hTERT-immortalized human foreskin fibroblasts (8), derived from ATCC HFF-1 cells
600 (SCRC-1041) were maintained in Dulbecco's modified Eagle's medium supplemented with
601 5%-10% newborn calf serum (Millipore Sigma) and antibiotics (complete DMEM) exactly as
602 described previously (8). i148^{HA} and i159^{HA} ARPE-19 epithelial cells (10), which upon
603 treatment with 100 ng/mL doxycycline, express HA-tagged UL148 or Rh159, respectively,
604 were likewise maintained in complete DMEM. For live cell imaging studies, i148^{HA} and
605 i159^{HA} ARPE-19 were maintained in Opti-MEM (Thermo Fisher) supplemented with 3%
606 certified tet-approved fetal bovine serum (FBS), 20 µg/mL gentamicin sulfate, 1 µg/mL
607 puromycin HCl and 10 µg/mL ciprofloxacin HCl. Telomerase-immortalized rhesus
608 fibroblasts (75) were a kind gift of Peter A. Barry, and were maintained in complete DMEM.
609 The acute monocytic leukemia cell line THP-1 (TIB-202) was obtained from ATCC
610 (Manassas, VA) and maintained as suspension cultures in RPMI 1640 medium
611 supplemented with 10% FBS (Millipore Sigma) and antibiotics (10 µg/mL ciprofloxacin and
612 25 µg/mL gentamicin). THP-1 were differentiated into adherent macrophages by incubating
613 for 48 h in the presence of 100 nM 2-O-tetradecanoylphorbol 13-acetate (Millipore Sigma),
614 and subsequently infected with the indicated viruses at an MOI of 5 $TCID_{50}$/cell.

615 Infectious bacterial artificial chromosome (BAC) clones of the following HCMV
616 strains were used for this study: TB40/E (also known as TB40-BAC4 or TB_WT) (11) as
617 well as its derivatives TB_148^{HA} and TB_148$_{STOP}$, which were used in our previous studies
618 (1, 8, 10); TR (TR*gfp*) (76, 77); Merlin repaired for *UL128* and *RL13* harboring *tetO*
619 sequences upstream of *UL131* (pAL1393) (78); AD169 repaired for *UL131* (AD_r131)(1,
620 79) and AD_r131_148^{HA}, a derivative of AD_r131 that carries a full length UL148 (from

621 strain TB40/E) tagged with an HA-epitope at the original *UL148* locus (8). An infectious
622 BAC clone of rhesus CMV (RhCMV) strain 68-1 (80) and a derivative that expresses an
623 HA-tagged Rh159 (details below) were also used for certain experiments.
624 The methods used for reconstitution of HCMV from purified BAC DNA, cultivation of virus
625 and preparation of stocks, including ultracentrifugation through sorbitol cushions and
626 determination of infectious titers by tissue culture infectious dose 50 ($TCID_{50}$) assay have
627 been described elsewhere (8, 10).
628
629 **Construction of recombinant viruses and new plasmids for the study.**
630 New recombinant viruses for this study were derived from BAC-cloned HCMV and
631 RhCMVs using *en passant* mutagenesis in GS1783 *E. coli,* a strain K12 derivative that
632 expresses the homing endonuclease I-SceI upon treatment with L-(+)-arabinose (81, 82).
633 Recombinant BACs were confirmed by Sanger DNA sequencing of the modified regions,
634 which was performed by Genewiz, Inc. (Piscataway, NJ) (not shown). Oligonucleotide
635 primers for construction of recombinant viruses and plasmids were custom synthesized by
636 Integrated DNA Technologies (Coralville, IA); sequences are provided in **Table S1**. Type II
637 restriction endonucleases, T4 DNA ligase, and Gibson assembly reagents (NEB HiFi
638 Assembly Master Mix) for generation of recombinant DNAs and for routine molecular
639 cloning and subcloning procedures were obtained from New England Biolabs (Ipswitch,
640 MA). KOD Hot Start DNA polymerase (EMD Millipore) was used for all PCR reactions.
641 To construct TB_159^{HA}, a strain TB40/E derivative in which the UL148 open reading
642 frame is replaced by Rh159 we carried out the following steps. Primers Rh159_Fw and
643 Rh159_HA_Rv were used to amplify and HA-tag the *Rh159* ORF from
644 pcDNA3.1+_Rh159_IRES_GFP (a gift from Klaus Früh, OHSU). The PCR product was
645 inserted into EcoRV-digested pEF1α using Gibson assembly. A PCR product containing

646 an ISce-I excisable kanamycin cassette was amplified from TB_148^{HA}_*ISce-Kan* integrate
647 BAC (1) using primers PpuISceKanGibs_Fw and PpuISceKanGibs _Rv and Gibson-
648 assembled into PpuMI-digested pEF1α_Rh159 plasmid to yield plasmid
649 pEF1α_Rh159_ISceKan. Primers Rh159_Fw_recomb and Rh159_Rv_recomb were used
650 to generate a PCR product from template plasmid pEF1α_Rh159_ISceKan. The PCR
651 product was electroporated into GS1783 E. coli harboring the TB_148^{HA} BAC, and Kan^{r}
652 colonies harboring TB_Δ148_Rh159_ISceKan integrate BACs were isolated on Luria-
653 Bertiani agar plates. Bacterial colonies representing kanamycin resistant integrates were
654 obtained and were subsequently resolved to 'scarlessly' remove the positive selection
655 marker by standard *en passant* protocols (81, 82) to yield TB_Δ148_Rh159^{HA}, which we
656 abbreviate herein as TB_159^{HA}. TB_159^{HA} was sequence-confirmed using primers
657 TB_159HAseq_F and TB_159HAseq_R. Similar strategies were used to modify the
658 RhCMV 68-1 BAC (80) to incorporate sequences encoding an HA-epitope immediately
659 before the stop codon of *Rh159*. An *en passant* strategy in which a shuttle plasmid
660 carrying *I-SceI-Kan^{r}* disrupted by in-frame nonsense codons was used insert premature
661 nonsense codons in the *UL148* CDS in the context of HCMV strains Merlin (pAL1393) and
662 TR (TR*gfp*), and was applied as described previously for generating TB_148$_{STOP}$, the
663 UL148$_{STOP}$ mutant of strain TB40/E (8).
664 To construct "tet-on" lentivirus vector plasmids containing UL148 fused to GFP, we
665 used primers Gibs_eGFP_Rv and 148_eGFP_Fw to amplify the GFP gene from a dsDNA
666 gBlock, EGFP-P2A-3XHA, synthesized by Integrated DNA Technologies (Coralville, IA),
667 which was a gift of Matthew D. Woolard (LSU Health Sciences Center, Shreveport, LA). In
668 a separate PCR, the *UL148* gene was amplified from plasmid pcDNA3.1-UL148^{HA} (10)
669 using primers Gib_148_Fw and 148_noStopRv. The two products were assembled, using

670 Gibson Assembly, together with EcoRV opened pcDNA3.1(+) (Invitrogen) to produce
671 pcDNA3.1-UL148-GFP. After confirming the absence of spurious mutations by Sanger
672 DNA sequencing (Genewiz, not shown), the *UL148-GFP* cassette from pcDNA3.1-UL148-
673 GFP was released by EcoRI and NotI digestion and ligated into pOUPc turboRFP-link
674 plasmid which had been linearized using the same restriction sites. pOUPc turboRFP-link
675 is a derivative of lentiviral vector pOUPc (10) that was constructed by reinsertion of
676 turboRFP (tRFP). Briefly, tRFP was amplified from the original pOUPc-turboRFP using
677 primer pair tRFP linker Fw and tRFP linker Rv and then reinserted by Gibson Assembly
678 with pOUPc turboRFP that had been double-digested using EcoRI and Not I in order to
679 linearize the vector and remove the *turboRFP* (RFP) sequence.
680 To express Rh159 fused to eGFP, primers Gibs_eGFP_Rv and 159_eGFP_Fw were
681 used to amplify the GFP gene from EGFP-P2A-3XHA, and in a separate PCR reaction,
682 primers Gibs_159_Fw and 159_noStop_Rv Rh159 were used to amplify *Rh159* from
683 pcDNA3.1-Rh159^{HA} (10). The latter two PCR products were assembled together with
684 EcoRV linearized pcDNA3.1(+) using Gibson Assembly, resulting in plasmid pcDNA3.1-
685 Rh159. The latter plasmid was used as template in a PCR reaction with primers
686 Gibs_Age_159_Fw and Gibs_Mlu_GFP_Rv. The resulting PCR product was Gibson
687 assembled into the lentiviral vector pOUPc (10) which had been double-digested with Mlu I
688 and Age I.
689
690 **Drug treatments.**
691 The PERK inhibitor, GSK2606414 (50), doxycycline hyclate, and folimycin were obtained
692 from MilliporeSigma (Burlington, MA). ISRIB (42-46) was obtained from MilliporeSigma or
693 APExBio (Boston, MA) and epoxomicin was procured Selleck Chemicals (Houston, TX).
694 ISRIB was dissolved in DMSO to make a 10,000× stock solution (2 mM) and used at a final

695 working concentration of 200 nM. GSK2606414 was dissolved in DMSO to make a
696 10,000× stock solution (11 mM) and used at a final working concentration of 1.1 μM.
697 Folimycin was prepared as a 1000× (115.46 μM) stock solution in DMSO and used at 115
698 nM final. Epoxomycin was prepared as a 100× (2 mM) stock solution in DMSO and used at
699 a final concentration of 20 μM.
700
701 **Confocal microscopy and live-cell imaging.** Confocal indirect immunofluorescence
702 microscopy imaging on fixed cells was carried out using Leica TCS SP5 Spectral Confocal
703 Microscope (Leica Microsystems, Heidelberg, Germany) using a Leica HCX PL APO CS
704 63x/1.4-0.6NA objective under oil immersion, except for the image shown in Figure 1C,
705 which was captured on a Nikon SIM-E and A1R confocal microscopy system (Nikon
706 Instruments, Melville, NY) using a Nikon SR Apo TIRF 100x/1.49NA objective under oil
707 immersion. Images for different fluorophore channels were acquired using sequential
708 scanning. Direct immunofluorescence live cell imaging data were collected using the Nikon
709 SIM-E microscope using a Nikon Apo 60x/1.40NA DIC objective. The 3D projection shown
710 in FIG 1 was generated by NIS-Elements AR Analysis 4.60.00 (64-bit) software (Nikon)
711 from Z-stacks captured on the Nikon SIM-E / A1R microscope using a Nikon SR Apo TIRF
712 100x/1.49NA objective. For FIG 11, 3D projections were generated by Imaris x64 9.3.0
713 software (Bitplane, Inc.) in maximum intensity projection (MIP) mode.
714 For fixed cell imaging experiments other than those shown in Fig S1D, cells were
715 seeded on 12 mm circular, No. 1 thickness microscope cover glass (200121; Azer Scientific,
716 Morgantown, PA). At the indicated times post-treatment and or post-infection, cells were
717 washed with phosphate buffered saline (PBS) [137 mM NaCl, 2.7 mM KCl, 10 mM Na_2HPO_4,
718 and 1.8 mM KH_2PO_4, pH 7.4]; fixed for 15 min at room temperature in PBS containing 4%
719 (wt/vol) paraformaldehyde (Fisher Scientific, Waltham, MA), washed in PBS, permeabilized

720 for 10 min using 0.1% Triton X-100 (in PBS), subsequently washed again in PBS, and then
721 blocked for 45 min at 37 °C in PBS containing 5% (vol/vol) normal goat serum (Rockland
722 Immunochemicals, Limerick, PA). Cells were then washed three times in PBS followed by
723 incubation in 1% Human Fc Block (BD Biosciences, San Jose, CA) in PBS, for additional 45
724 min at 37 °C. Cells were then incubated in the presence of primary antibodies for 1 h at 37
725 °C or 4 °C overnight, and then washed three times with PBS containing 0.1% Tween-20
726 (PBST) for 5 min per wash. Alexa Fluor-labeled goat polyclonal secondary antibodies (all
727 from ThermoFisher Invitrogen, Waltham, MA, see **Table S2**) were used for secondary
728 detection. The slides were then mounted using Prolong Gold anti-fade reagent containing
729 DAPI (ThermoFisher) and placed under a Leica TCS SP5 confocal microscope for image
730 acquisition using a Leica 63× oil immersion objective lens (Leica Microsystems, Buffalo
731 Grove, IL).

732 For indirect immunofluorescence staining results of primary clinical isolates (SI Fig
733 S1D), four clinical HCMV isolates obtained by routine testing of throat swabs from patients
734 of the Ulm University Medical Center were provided by the diagnostic laboratory of the
735 Institute of Virology in Ulm. Sample material was applied to human fibroblasts and incubated
736 for several days until HCMV-positive cells could be detected. Infected cells were then seeded
737 together with uninfected fibroblasts, incubated for up to 5 days until plaques were formed
738 and processed for indirect immunofluorescence staining. ERQC compartments were
739 detected by staining for calnexin (CNX, E10; Santa Cruz Biotechnology, mouse, 1:50
740 dilution), the cVAC was detected by staining for HCMV pUL71 (rabbit, 1:500). Secondary
741 antibody used for detection of CNX was Alexa Fluor 555 labeled goat anti-mouse IgG
742 (1:1000) and for pUL71 detection, Alexa Fluor 488 conjugated goat anti-rabbit IgG (1:1000).
743 Confocal images were acquired using the 63× objective of a Zeiss Observer Z1 fluorescence

744 microscope equipped with Apotome and Zen software 2.3 (Carl Zeiss Microscopy GmbH,
745 Jena, Germany).
746
747 **FRAP.** FRAP studies were carried out on using live ARPE-19 cells from the i148^{GFP} and
748 i159^{GFP} populations as follows. Cells were seeded as above for live-cell imaging, induced
749 for transgene expression using dox (100 ng) for 24 h, and then placed on an incubated
750 sample stage of a Nikon A1R SIM-E imaging system equipped with an SR Apo TIRF
751 100x/1.49NA objective (Nikon). Three rectangular regions in image fields were defined for
752 measurement of (i) background signal, and of two regions with comparable initial GFP
753 signals, (ii) one designated as a control region (no photobleaching) and another for (iii)
754 photobleaching and recovery of signal after photobleaching. Photobleaching of selected
755 regions was carried out for 20 s using 405 nm laser light from a LU-N4 laser fiber (Nikon)
756 [power at source: 15 mW, power at objective: 8 mW]. Images and signal intensity
757 measurements were captured every 2 s at a rate of 1 frame per s (488 nm excitation, FITC
758 channel) starting immediately before photobleaching (t=1), and from t=20 s to t=320 s after.
759
760 **Electron microscopy.** Procedures to prepare samples for transmission electron microscopy
761 (TEM) included high-pressure freezing (HPF), freeze substitution, and Epon embedding,
762 which were carried out as described previously (83). Briefly, human fibroblasts were seeded
763 in µ-Slides (Ibidi GmbH, Martinsried, Germany) containing carbon-coated sapphire discs
764 (Engineering Office M. Wohlwend GmbH) 1 day prior to infection at 80 to 90% confluence.
765 Cells were infected with virus overnight at MOI 1. Medium containing viral inocula was
766 replaced with fresh medium the next day. Infected cells on sapphire discs were fixed by using
767 HPF with a Compact 01 high-pressure freezer (Engineering Office M. Wohlwend GmbH,
768 Sennwald, Switzerland) at 5 dpi. Thereafter, cells on sapphire discs were processed by

769 freeze-substitution and subsequently embedded in Epon (Fluka, Buchs, Switzerland).
770 Ultrathin sections of the Epon-embedded cells were cut with an ultramicrotome (Ultracut
771 UCT; Leica Microsystems, Wetzlar, Germany) and placed on Formvar-coated single-slot
772 grids (Plano GmbH, Wetzlar, Germany). Grids were examined in a Jeol JEM-1400 (Jeol Ltd.,
773 Tokyo, Japan) transmission electron microscope equipped with a charge-coupled-device
774 (CCD) camera at an acceleration voltage of 120 kV. Fixation and embedding of infected
775 cells for scanning transmission electron microscopy (STEM) tomography was the same as
776 described for TEM. Additional sample preparation steps were conducted as described
777 previously (84, 85). Tomogram acquisition was conducted on a STEM Jeol JEM-2100F with
778 an acceleration voltage of 200 kV. Tilt series were acquired from 600 nm thin sections from
779 +72° to -72° with a 1.5° increment using the bright field detector. Image series were
780 reconstructed to tomograms by weighted back projection with the IMOD software package
781 (86). 3D visualization of the membrane structures was performed using Avizo lite software
782 (Visualization Science Group, Burlington, MA, USA) by threshold segmentation.
783
784 **Western blotting.** Western blotting procedures, including primary and secondary
785 antibodies used for detection of HA tag, UL148, ATF4, eIF2α, P-eIF2α (Ser51), the HCMV
786 viral nuclear antigen IE1, and the conditions used for detection of Ser51 phosphorylated
787 eIF2α, were carried out as described previously (8, 10). Additional antibodies used in this
788 study were mouse anti-GAPDH (Cat. No. 60004-1, Proteintech, Rosemont, IL,), mouse
789 anti-gB clone 27-180 (87) (a generous gift of William J. Britt), and anti-GFP (D5.1) XP®
790 Rabbit mAb #2956 (Cell Signaling Technology, Danvers, MA).
791
792 **Solubility analyses.** 2.0×10^5 human fibroblasts were infected at an MOI of 1 $TCID_{50}$ per
793 cell with TB_148^{HA} or TB_159^{HA}. The following day, cells were washed twice with PBS to

794 remove viral inoculum and replenished with DMEM containing 5% newborn calf serum. At
795 the indicated times post-infection, cells were washed once with PBS and lysed by direct
796 addition of 100 μL RIPA buffer [25 mM HEPES (pH 7.5), 400 mM NaCl, 0.1% SDS, 0.5%
797 sodium deoxycholate, 1% NP-40, supplemented with 1× protease inhibitor cocktail
798 (ApexBio)]. Lysates were collected and rotated at 4˚C for 1 h. Insoluble material was
799 pelleted by centrifugation (21,000 × *g*, 35 min). Supernatants containing soluble material
800 were transferred to a fresh microfuge tube, and 33 μL of 4× Laemmli sample buffer [200
801 mM Tris (pH 6.8), 8% SDS, 40% glycerol, 0.08% bromophenol blue] was added to bring
802 final volume to 133 μL. The pellet was disrupted in 133 μL of 1X Laemmli buffer prepared
803 by diluting 4× Laemmli buffer in RIPA buffer. Samples were reduced by addition of beta-
804 mercaptoethanol (5% final, v/v) and boiled at 90˚C for 10 min. 40 μL of each sample was
805 resolved by SDS-PAGE (12% polyacrylamide gel), transferred overnight to nitrocellulose
806 membrane, and immunoblotted with antibodies against HA epitope or HCMV gB.
807 Quantitation of secondary antibody fluorescence signals were performed using an Odyssey
808 CLx scanner (Li-Cor, Inc., Lincoln, NE) in auto-scan mode. For each time-point, the signals
809 from RIPA-soluble and insoluble bands were summed to yield total signal, and the ratio of
810 insoluble band signal to total signal were also reported as percent insoluble HA over total
811 HA signal.
812
813 **Statistical analyses.** Statistical analyses were carried out using GraphPad Prism 8.1.0 for
814 MacOS (GraphPad, Inc., San Diego, CA).
815
816 **ACKNOWLEDGEMENTS.**

817 This project was supported by NIH grants R01-AI116851 (to J.P.K.) and P30-
818 GM110703. Its contents are solely the responsibility of the authors and do not necessarily
819 represent the official views of the NIAID or the NIGMS.
820 We are especially grateful to Erik L. Snapp (HHMI, Janelia Laboratories) for helpful
821 discussions and advice on interpretation of EM and confocal image data. We also thank
822 the following individuals for generously sharing reagents: Dong Yu (Washington University,
823 St. Louis, MO, currently GSK Vaccines), Thomas E. Shenk (Princeton University,
824 Princeton, NJ), Richard J. Stanton (Cardiff University, United Kingdom), William J. Britt
825 (University of Alabama, Birmingham), W. L. William Chang and Peter A. Barry (both of the
826 University of California, Davis; Davis, CA), Christian Sinzger (University Medical Center
827 Ulm, Ulm, Germany), Klaus Früh (Oregon Health Sciences University, Beaverton, OR), and
828 Gregory A. Smith (Northwestern University, Chicago, IL).
829

830 **AUTHOR CONTRIBUTIONS.**

831 Performed experiments: HZ, CR, CCN, MNAS, JvE. Data analysis and interpretation: HZ,
832 CR, CCN, JvE, CS, JPK. Designed experiments: HZ, CR, CCN, JvE, and JPK. Contributed
833 new reagents: HZ, CH, CCN, JPK. Electron microscopy and STEM tomography: CR and
834 JvE. Obtained funding: JPK. Wrote the manuscript: JPK with comments from JvE and CR.

835 **FIGURES.**

836

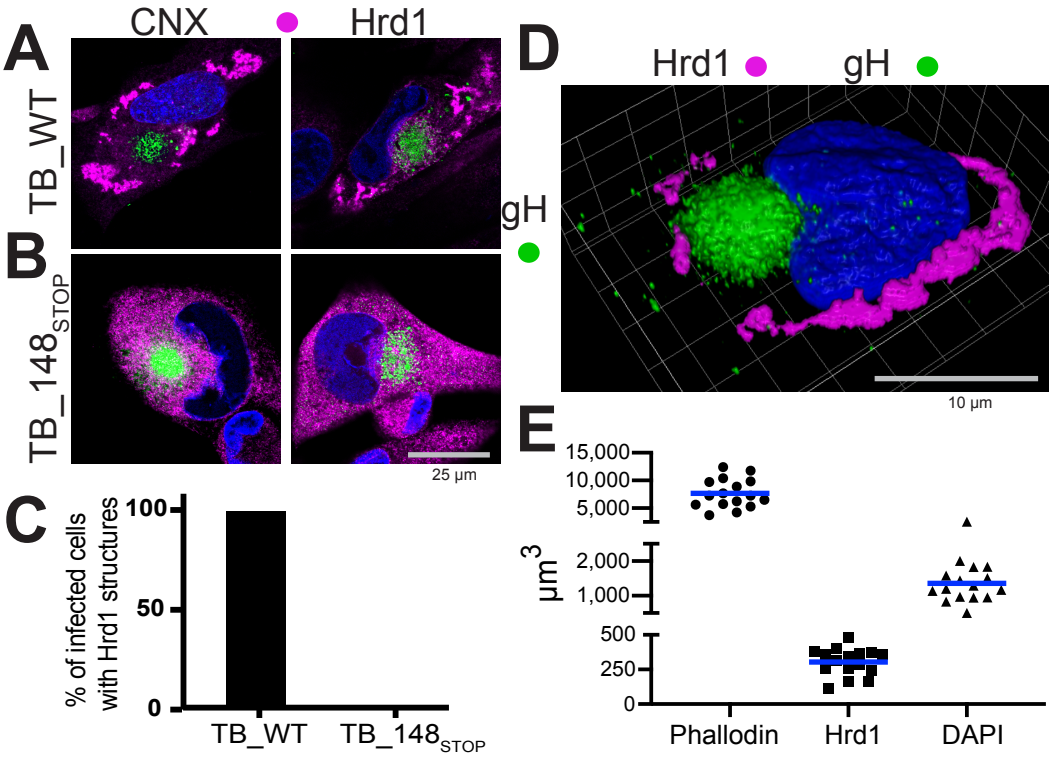

837
838

839 **FIG 1. UL148 reorganizes ER markers into anomalous structures during HCMV infection.**
840 Fibroblasts infected at MOI 1 $TCID_{50}$/cell with either **(A)** wildtype HCMV strain TB40/E (TB_WT) or
841 **(B)** an isogenic *UL148*-null mutant (TB_148_{STOP}), were fixed at 96 h postinfection (hpi) and imaged
842 by confocal microscopy after staining with antibodies specific for calnexin or Hrd1 (magenta) and
843 glycoprotein H (gH, green), as indicated. DAPI (blue) signal was used to counterstain nuclei. **(C)**
844 Percentage of fibroblasts that contain Hrd1 structures at 96 hpi; fifty gH-positive cells for each
845 condition were scored for the presence or absence of UL148 structures (also see SI Fig S1A). (**D**)
846 3D confocal image projection of a TB_WT infected fibroblast stained at 96 hpi for Hrd1 and gH. **(E)**
847 Volumetric measurements were made from sixteen infected cells, stained with phalloidin-AlexaFluor
848 594 conjugate to estimate total cell volume, with Hrd1 antibody to estimate the volume of UL148-
849 dependent ER structures, and with DAPI to estimate nuclear volume.
850
851
852
853
854

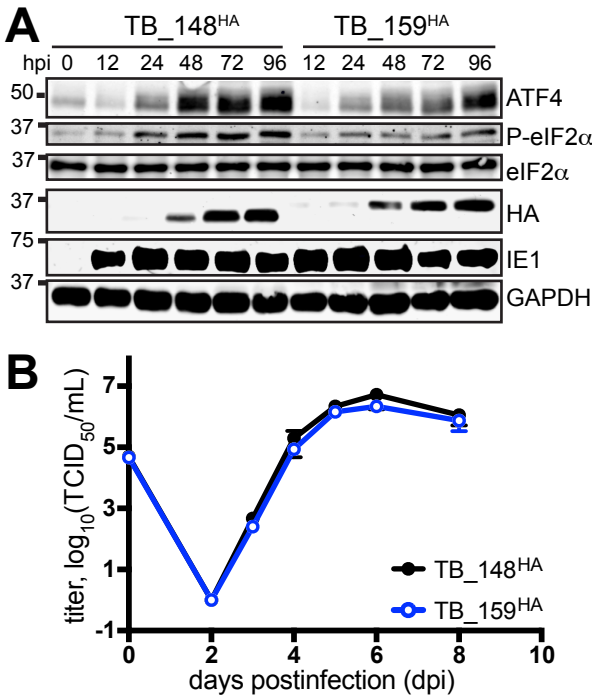

855
856
857 **FIG 2. Characterization of TB_148^{HA} and TB_159^{HA} viruses. (A)** Human fibroblasts were infected
858 at MOI 1 with the indicated recombinant HCMVs. Cell lysate samples harvested at the indicated
859 times postinfection (h postinfection, hpi) were analyzed by Western blot to detect HA-tagged UL148
860 or Rh159, the 72 kD viral nuclear antigen IE1-72 (IE1), and GAPDH. **(B)** Single-cycle viral replication
861 kinetic curves from MOI 1 infected fibroblasts were plotted by determining the titer in tissue culture
862 infectious dose 50 ($TCID_{50}$) from supernatants collected at the indicated times postinfection.

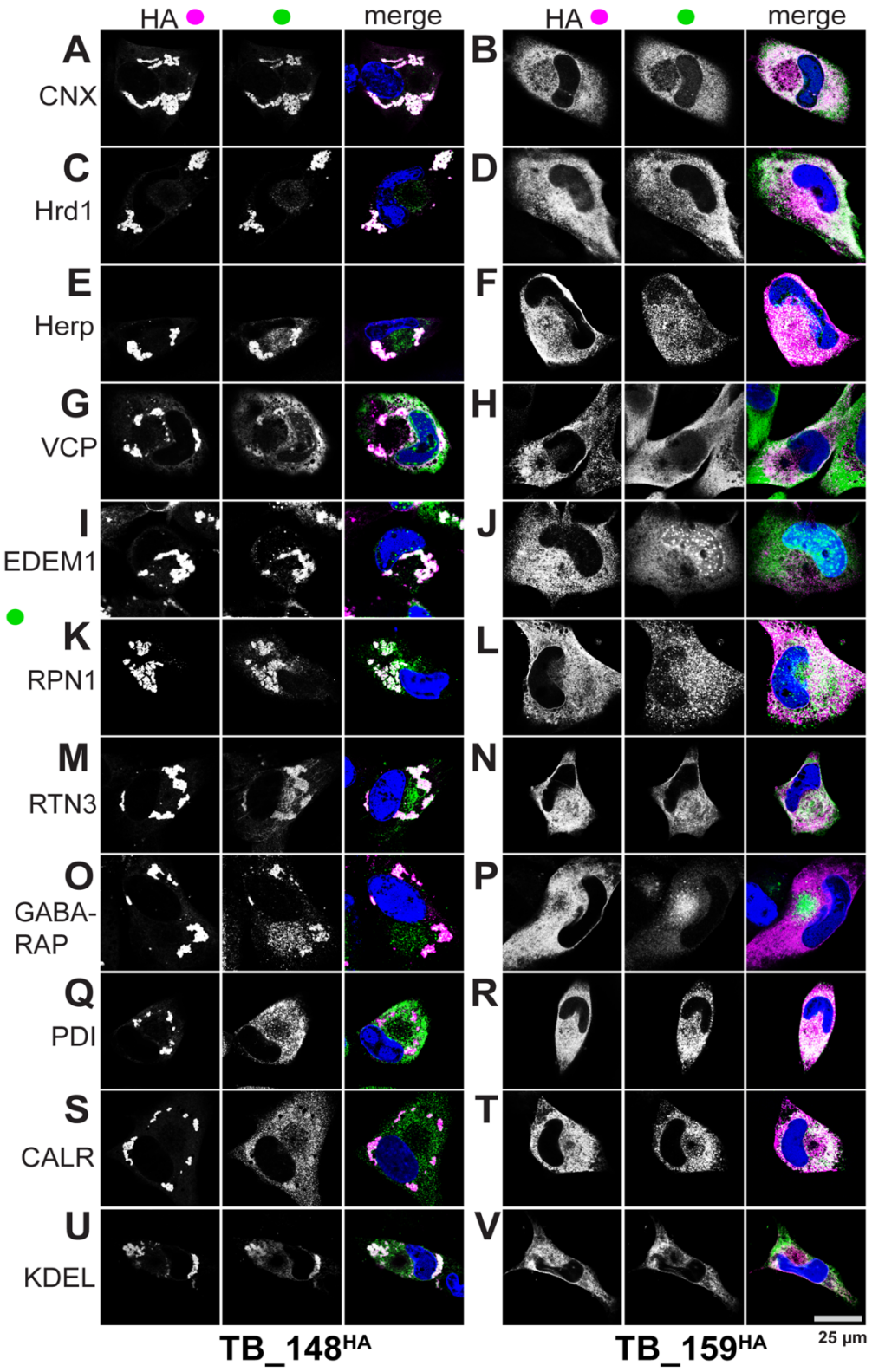

FIG 3. UL148 localizes to unusual ER compartments that are enriched for glycoprotein quality control markers. Fibroblasts infected at MOI 1 with either TB_148^{HA} (panels: **A, C, E, G, I, K, M, O, Q, S, U**) or TB_ 159^{HA} (panels: **B, D, F, H, J, L, N, P, R, T, V**) were fixed at 96 h postinfection, and imaged by confocal microscopy after co-staining with antibodies specific for HA (UL148 / Rh159, magenta in merge) and the indicated cellular markers (green in merge). DAPI (blue) counterstaining is shown in merged image.

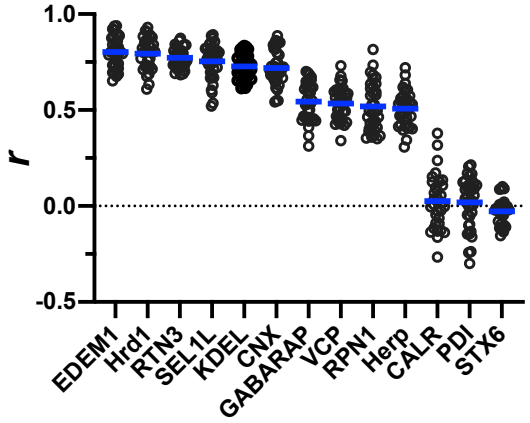

871
872
873 **FIG 4. Quantification of co-localization between UL148 and cellular markers.** A Pearson's
874 correlation coefficient (*r*) was calculated using NIH ImageJ software to estimate the degree of co-
875 localization between UL148 (HA signal) and each of the indicated cellular markers. A minimum of 30
876 cells were analyzed per marker. The arithmetic mean for each co-localization analysis result is shown
877 as a blue line, and data points for individual cells analyzed are plotted as circles.
878

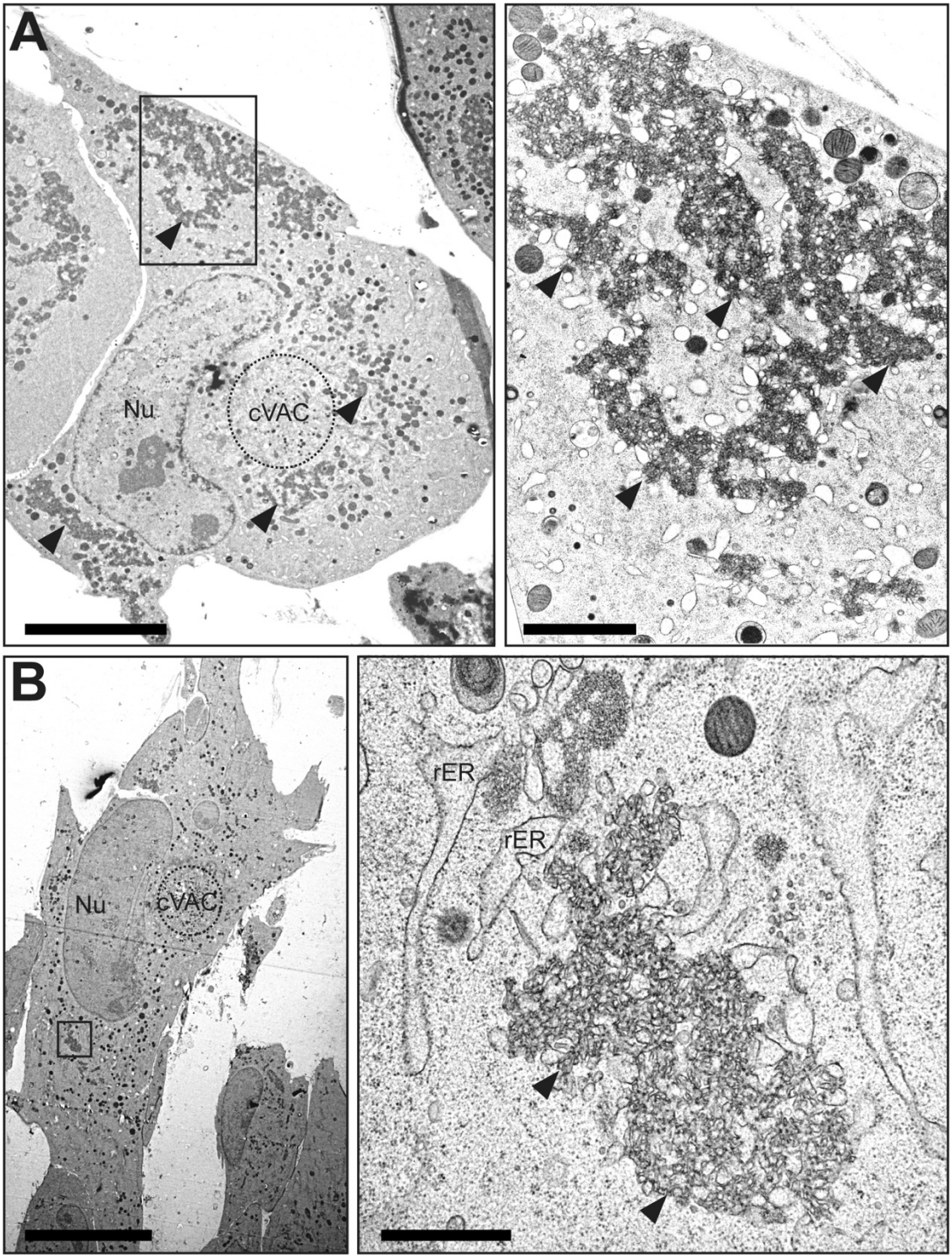

FIG 5. TEM of ER structures in wild-type HCMV infected cells. Human fibroblasts infected with wildtype HCMV (TB_WT) were fixed by high-pressure freezing and freeze substitution at day 5 postinfection and imaged using TEM. Panels (**A**) and (**B**) show cell overview at left. For each cell, the boxed region is shown at higher magnification. Scale bars; left panels: 10 µm, right panels: 2 µm. rER: rough ER; Nu: nucleus; cVAC: cytoplasmic viral assembly compartment. Solid arrowheads indicate the UL148-dependent ER structures of interest.

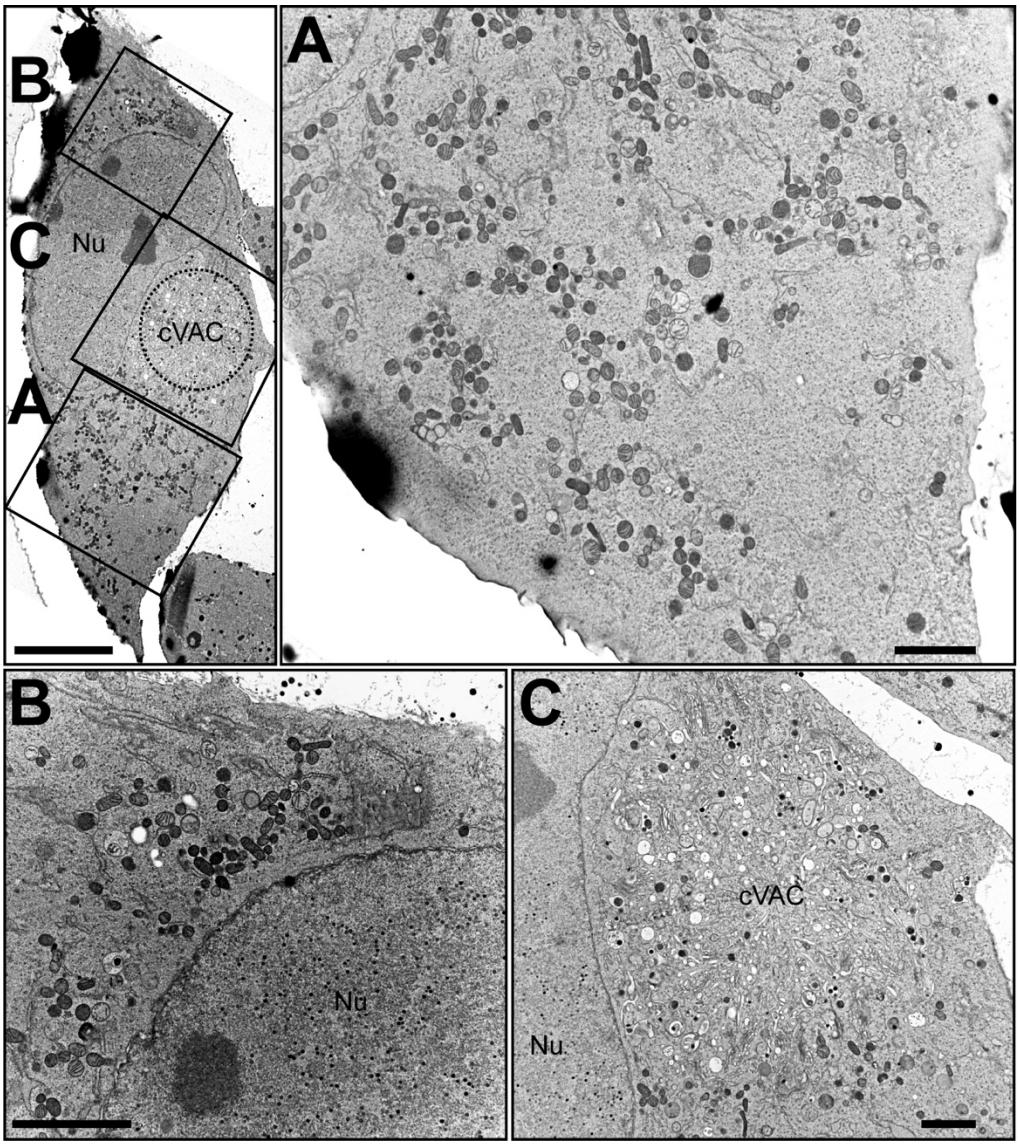

FIG 6. TEM of *UL148*-null HCMV infected cells. Human fibroblasts infected with a *UL148*-null mutant (TB_148$_{STOP}$) were fixed by high-pressure freezing and freeze substitution at day 5 postinfection and imaged using TEM. At the upper left an overview panel of a representative cell is shown with panels (**A**), **(B)**, and **(C)** each boxed. The boxed regions are expanded at higher magnification at right (**A**) and below (**B, C**). Scale bars for upper left overview panel: 10 µm, for zoomed panels: 2 µm. rER: rough ER; Nu: nucleus; cVAC: cytoplasmic viral assembly compartment.

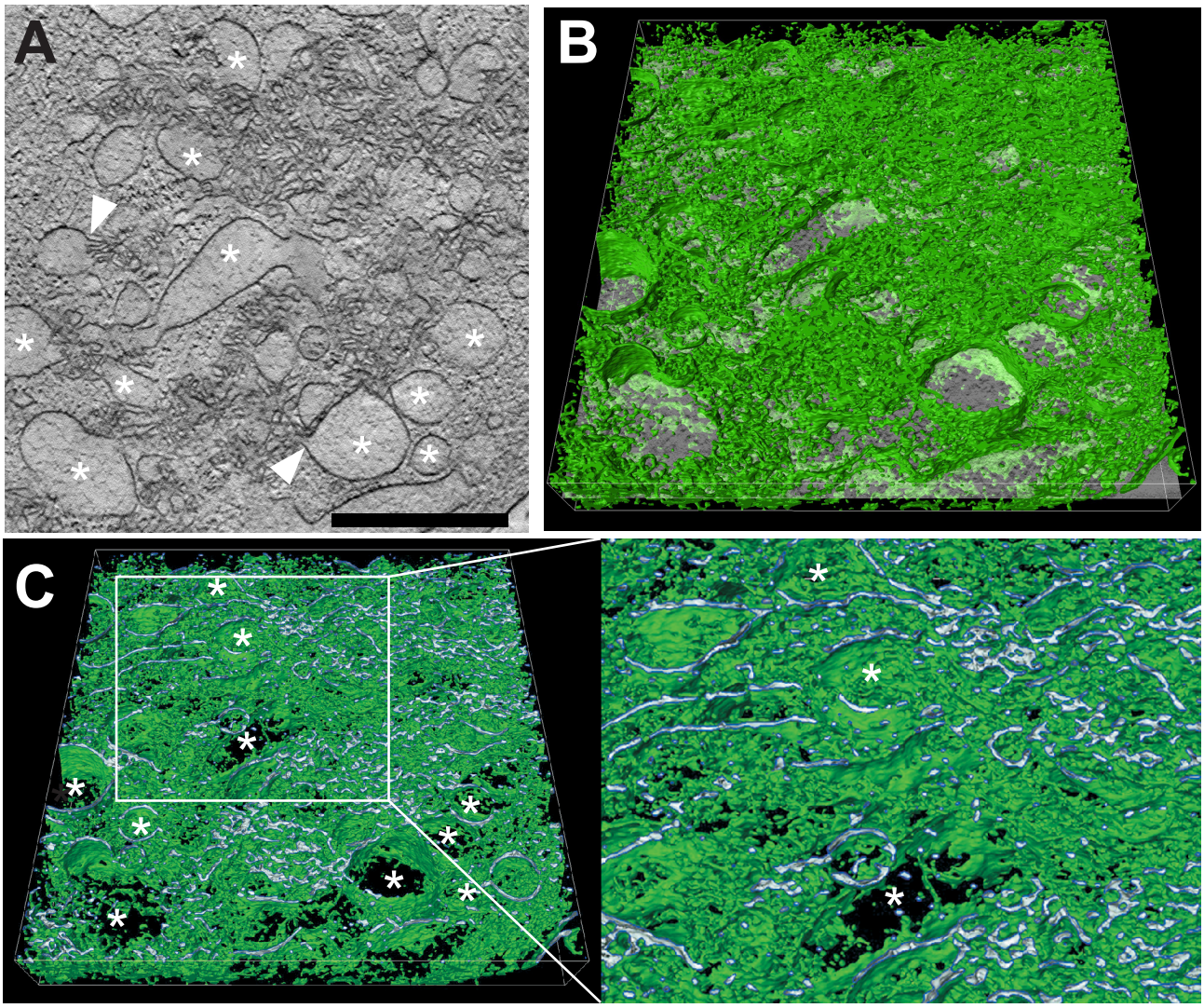

FIG 7. STEM tomography of UL148-dependent ER structures in HCMV infected cells. Human fibroblasts infected with wildtype HCMV (TB_WT) were fixed by high-pressure freezing and freeze substitution at day 5 postinfection and tomograms were recorded by STEM. (**A**) Shows a virtual section through the tomogram of a virus-induced membranous structure; asterisks denote ER structures of distended lumenal space. White arrowheads indicate sites at which membranes originating from distended ER cisternae continue into areas of involuted collapsed ER. Scale bar: 1 µm. (**B**) Shows the same virtual section as in (A) tilted and with a 3D visualization of the membranous network (green) of the entire tomogram. The same distended ER cisternae as in (A) are marked by asterisks. (**C**) Shows a cross section through (B) to visualize the membrane profile of the membranous structures. The region delimited by a white box is shown in a higher magnification on the right. Finer detail of the enlarged ER cisternae and the connections between them are readily visible; asterisks indicate the same distended ER cisternae as in panels (A) and (B). Also, see SI Movie S1. Scale bar: 1 µm.

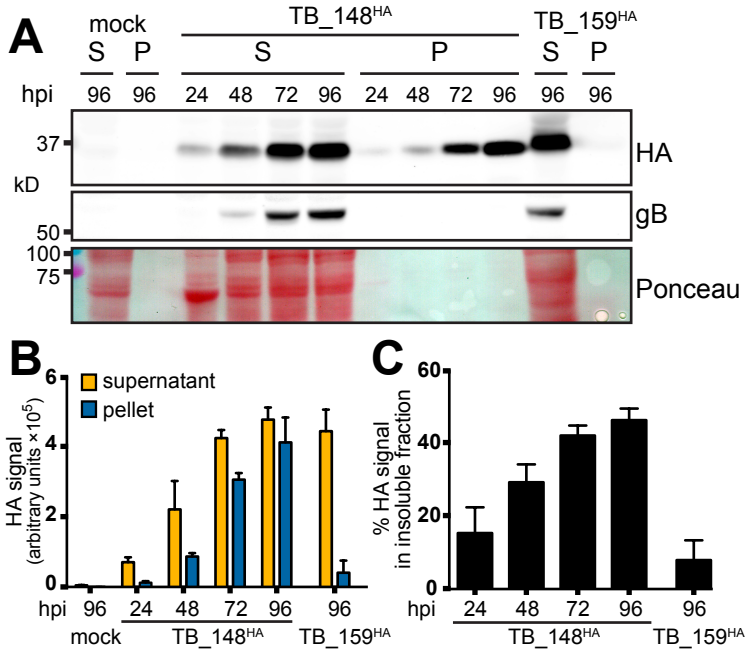

FIG 8. Solubility analysis of UL148 and Rh159. (**A**) Human fibroblasts were infected at MOI 1 $TCID_{50}$/cell with HCMV strain TB40/E derived viruses TB_148^{HA}, which expresses UL148 fused at its C-terminus to an HA-epitope tag, or TB_159^{HA}, which lacks *UL148* and instead expresses rhesus CMV Rh159 carrying a C-terminal HA tag. At the indicated times postinfection (hpi), infected cells were collected in radioimmunoprecipitation (RIPA) lysis buffer, centrifuged at 21,000 × *g* for 30 min, after which supernatant (S) and pellet (P) fractions were boiled in gel loading buffer containing 2% sodium dodecyl sulfate (SDS). Equivalent portions of supernatant and pellet were resolved by SDS-polyacrylamide gel electrophoresis, transferred to a nitrocellulose membrane for detection of protein species immunoreactive to antibodies against HA epitope (HA) and HCMV glycoprotein B (gB) and for total protein signal using Ponceau S reagent (Ponceau). (**B-C**). Signal intensity of fluorophore-conjugated secondary antibodies in anti-HA Western blots were measured from three independent biological replicates of the experiment shown in (A); error bars indicate standard deviation. (**B**) The fluorescent signal for each infection time point condition (y-axis is in arbitrary units, in hundred thousands). (**C**) The amount of signal found in the insoluble (pellet) fraction relative to the total signal (pellet plus supernatant) for each infection time point are plotted as percentage values.

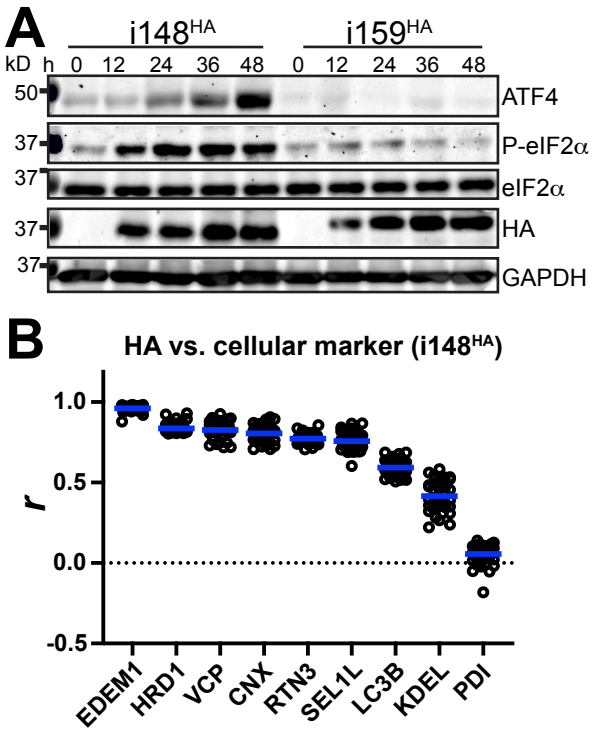

FIG 9. ISR activation accompanies redistribution of ER markers during ectopic expression of UL148. (A) Lysates of 'tet-on' ARPE-19 cells expressing either UL148 or Rh159 fused to an HA tag, i148^{HA} and i159^{HA}, respectively, were collected at the indicated times post doxycycline (dox) induction and analyzed by Western blot for the expression of the indicated proteins and for the abundance of eIF2α phosphorylated at Ser51 (P-eIF2α) using a phospho-specific antibody. (**B**) Pearson's correlation coefficient (*r*) values were calculated using NIH ImageJ software estimate the degree of co-localization between UL148 (HA signal) and the indicated cellular markers. A minimum of 30 cells were analyzed per marker. Arithmetic means for each co-localization analysis result are shown as blue lines, and data points for individual cells analyzed are plotted as circles.

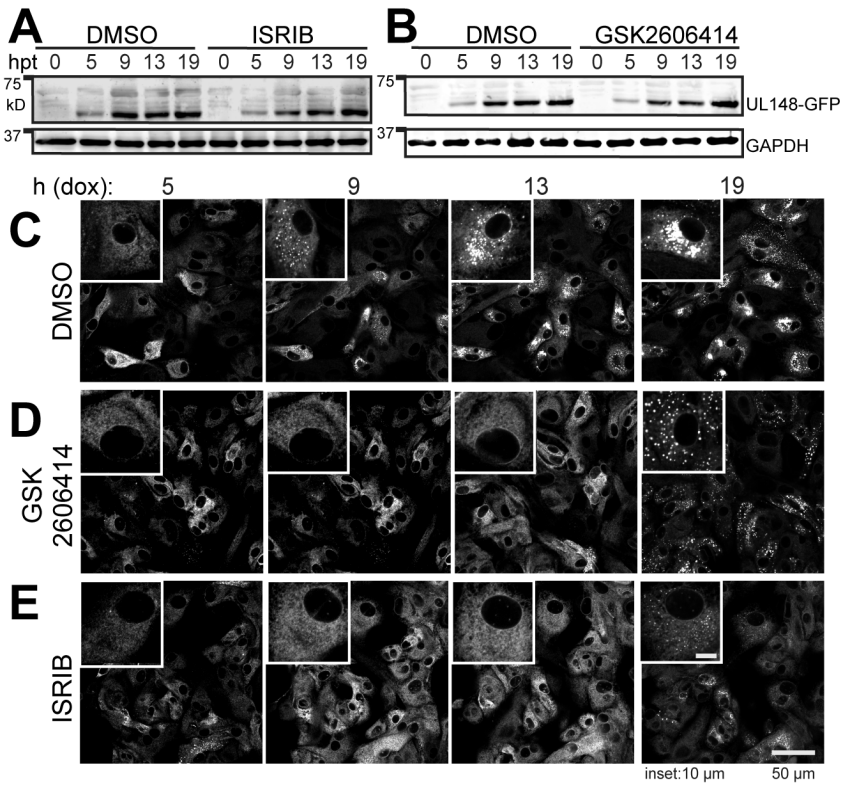

FIG 10. Inhibition of the integrated stress response impedes UL148-mediated ER remodeling. (A-B) "Tet-on" ARPE-19 epithelial cells that inducibly express UL148 fused to green florescent protein (gfp), i148^{gfp}, were induced for transgene expression using 100 ng/mL doxycycline (dox) in the presence of DMSO carrier, ISRIB (200 nM), or GSK2606414 (1.1 µM) and monitored by anti-UL148 Western blot for expression of UL148-GFP over a series of time points (h post treatment with dox, hpt). (**C-E**) Live cell imaging of UL148-GFP expression patterns in the presence of ISRIB (200 nM), GSK2606414 (1.1 µM), or DMSO vehicle (0.01%). Main scale bar represents 50 µm. For inset panels at upper left of each image, which are magnified 2.4× relative to the main image, the scale bar represents 10 µm. Also see SI Movies S8-S10.

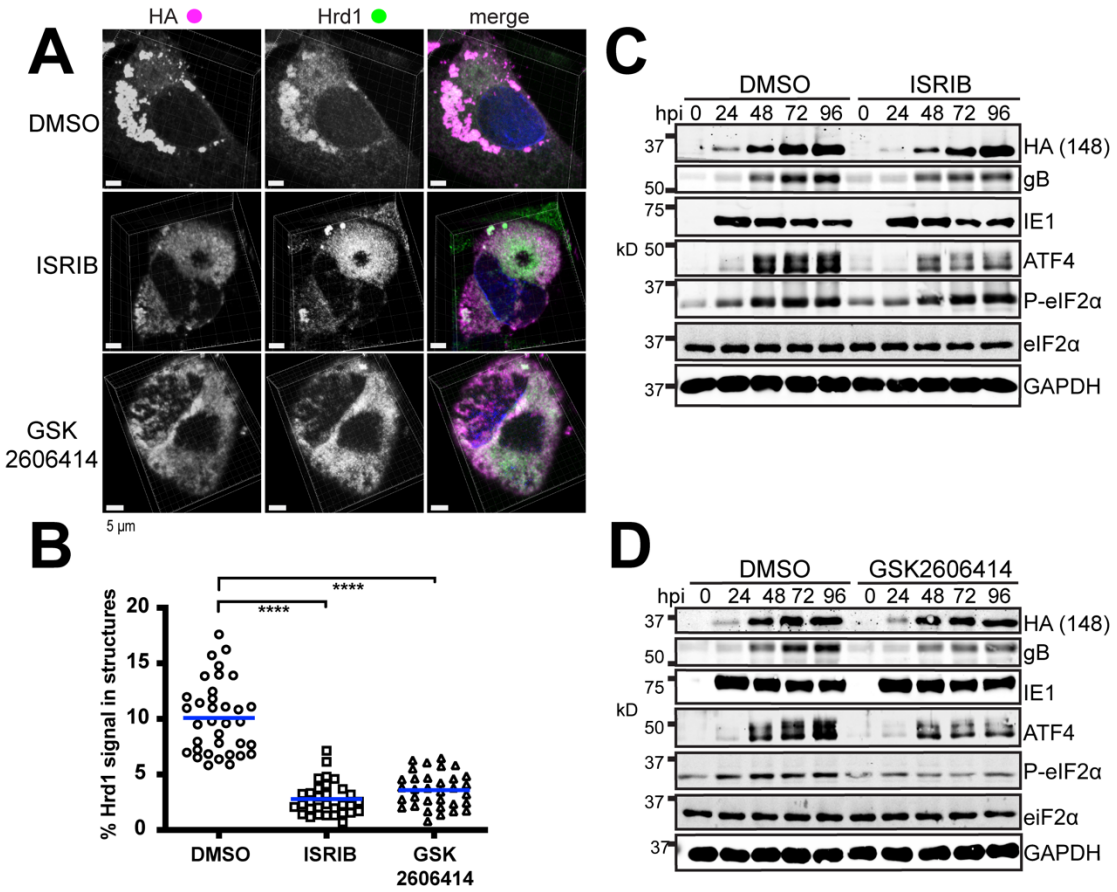

FIG 11. Inhibition of the ISR prevents the coalescence of Hrd1 and UL148 into discrete structures during infection. (**A**) Representative 3D maximum intensity projections of confocal imaging Z-stacks obtained from cells infected at MOI 1 for 96 h with HCMV strain TB40/E carrying HA-tagged *UL148* (TB_148^{HA}) and maintained in the presence of ISRIB (200 nM), GSK2606414 (1.1 µM), or DMSO carrier alone (0.1% vol/vol). In merged images HA signal is shown in magenta, Hrd1 in green, and DAPI counterstaining in blue. (**B**) The percent of Hrd1 antibody signal involved in discrete structures at 96 hpi were calculated for a minimum of 30 cells per condition using Imaris x64 9.3.0 software. Statistical significance was determined using a one-way ANOVA followed by Tukey's post-test; **** represents a P-value of <0.0001. The arithmetic mean for co-localization analysis results are shown as blue lines with data points for individual cells analyzed plotted as circles, squares or triangles, as indicated. (**C-D**) Western blot analyses of fibroblasts infected at MOI 1 with TB_148^{HA} and maintained in the presence of ISRIB (200 nM), GSK2606414 (1.1 µM), or DMSO carrier alone (0.01%); hpi: h post infection (hpi). Note: a phospho-specific antibody was used for detection of eIF2α phosphorylated at Ser51 (P-eIF2α).

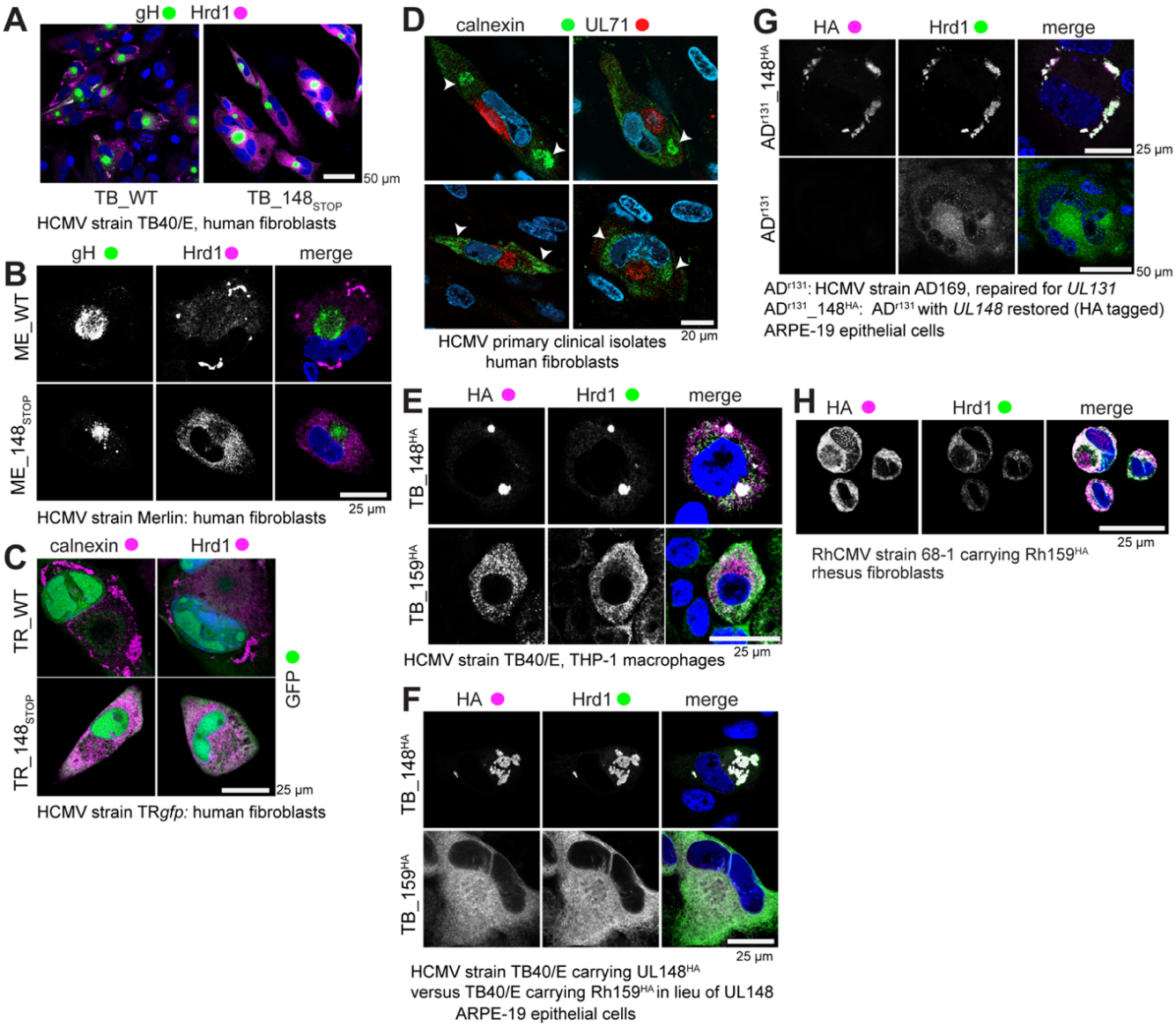

FIG S1: **Additional confocal microscopy results from infected cells.** (**A**) Lower magnification overview of results from FIG 1A-B; staining of gH and Hrd1 human fibroblasts 96 h postinfection (hpi) with wildtype HCMV strain TB40/E (WT) or *UL148*-null derivative TB_148$_{STOP}$. (**B**) gH and Hrd1 in human fibroblasts 96 hpi with either wildtype strain Merlin recovered from BAC pAL1393 (ME_WT) or a *UL148*-null derivative of the same virus (ME_148$_{STOP}$). (**C**): gH and Hrd1 at 96 hpi of human fibroblasts with wildtype HCMV strain TRgfp recovered from BAC-cloned TRgfp (TR_WT) or a *UL148*-null derivative of the same virus (TR_148$_{STOP}$). (**D**) Staining of the viral tegument protein UL71 and calnexin in human fibroblasts 5 days postinfection with primary clinical HCMV isolates obtained from patient throat swabs. (**E**) HA and Hrd1 in THP-1 macrophages fixed 96 hpi with HCMV strain TB40/E derivative viruses TB_148^{HA} or TB_159^{HA}. (**F**) HA and Hrd1 in ARPE-19 epithelial cells infected for 96 h with TB_148^{HA} or TB_159^{HA}. (**G**) Staining of HA and Hrd1 in ARPE-19 infected for 96 h with HCMV strain AD169 repaired for *UL131* and to which an HA-tagged *UL148* from TB40/E was restored to the native *UL148* locus (AD^{r131}_148^{HA}) versus parental AD169 repaired for *UL131* (AD^{r131}). Notes: (i) *UL131* is required for efficient infection of epithelial cells; (ii) for ADr131 we did not employ a viral marker (e.g., HA) to identify infected cells, so the appearance of syncytia and the characteristic kidney-bean shaped nucleus was used to indicate infected cells and a slightly lower magnification was used to best show these features. (**H**) HA and Hrd1 in telomerase-immortalized rhesus fibroblasts infected with BAC-derived rhesus CMV (RhCMV) strain 68-1 carrying an HA-tag at the C-terminus of Rh159.

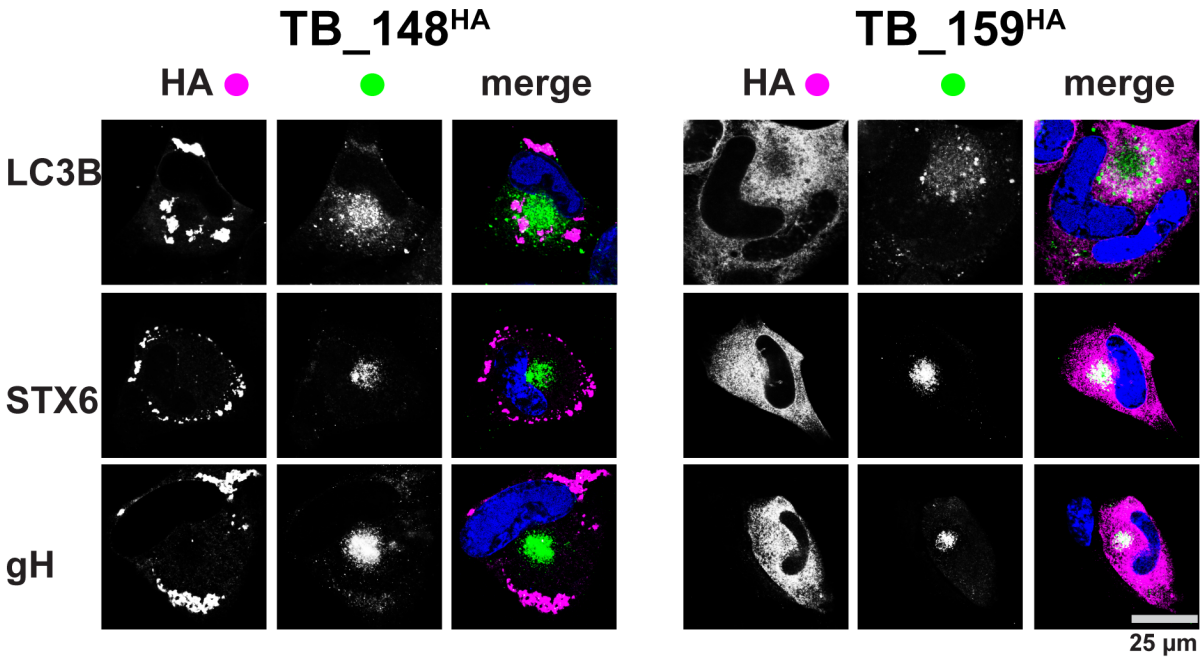

1003
1004
1005 **FIG S2: LC3B, syntaxin-6, and gH staining in HCMV infected cells.** Human fibroblasts were
1006 infected with the indicated viruses for 96 h and then fixed, permeabilized, and stained using
1007 antibodies specific for the indicated proteins. Indirect immunofluorescence images were captured
1008 using a 63X objective on a Leica SP5 confocal microscope. gH: glycoprotein H, STX6: syntaxin-6.
1009

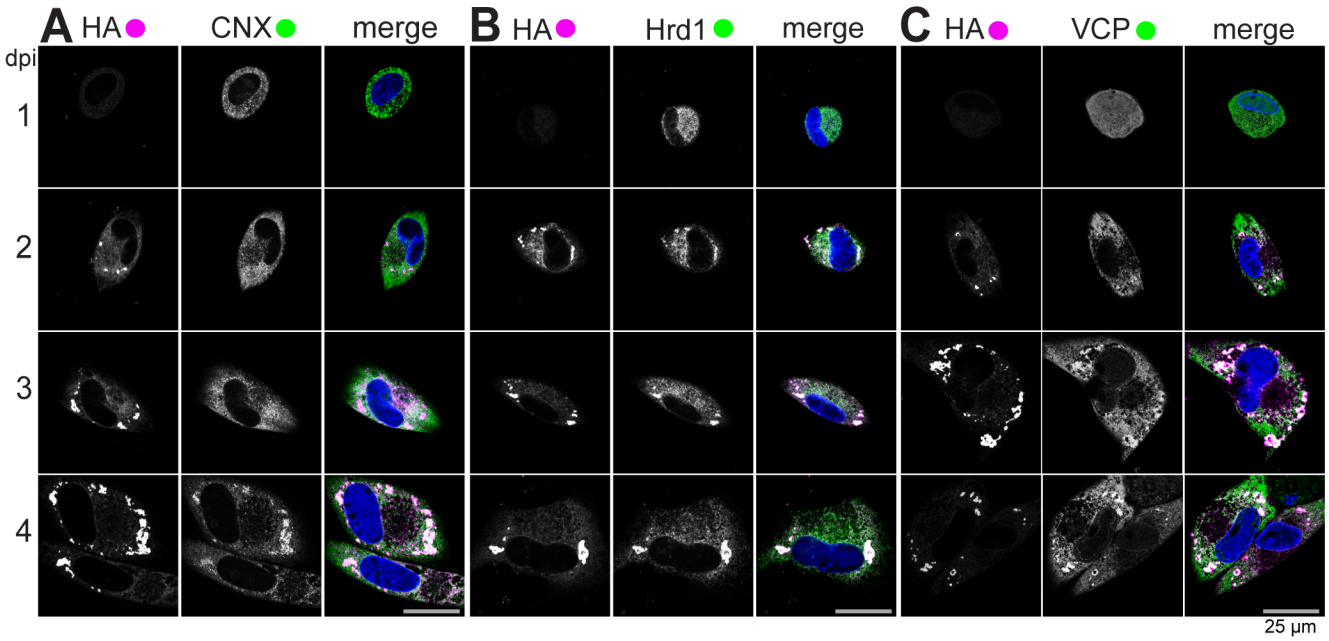

FIG S3: Cellular proteins involved in glycoprotein quality control are recruited with differing kinetics to UL148 ER structures. Fibroblasts infected with TB_148^{HA} at 1 MOI were fixed at the indicated time points (days post infection, dpi) and imaged by confocal microscopy after staining with antibodies specific for HA (UL148, magenta), CNX (green, **A**) , Hrd1 (green, **B**) or VCP(green, **C**), DAPI (blue).

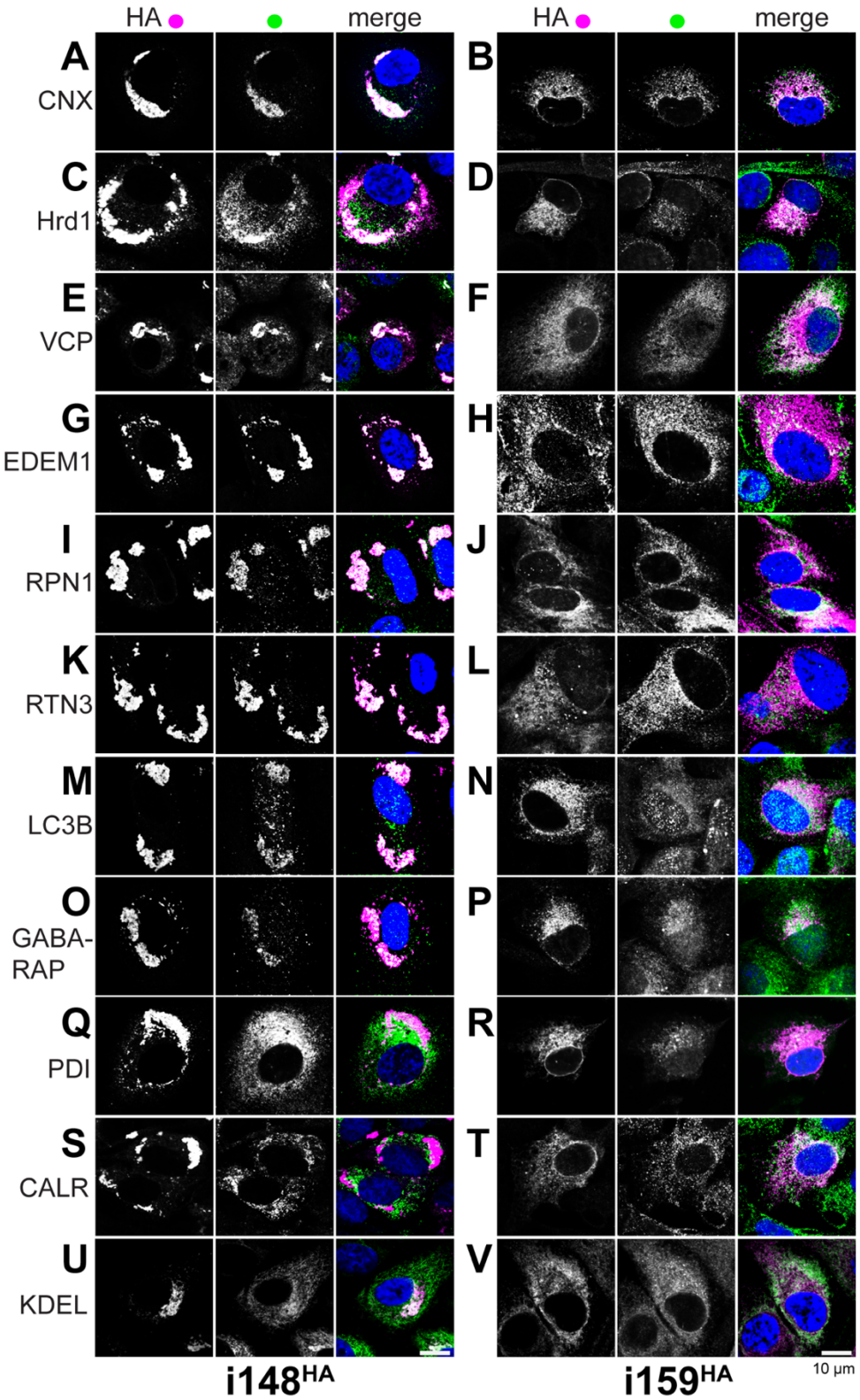

1018
1019 **FIG S4. UL148 is sufficient to remodel the ER.** Expression of HA-tagged UL148 or Rh159 was
1020 induced in "tet-on" ARPE-19 epithelial cells, i148^{HA} and i159^{HA}, respectively. Cells were fixed at 48
1021 h postinduction for indirect immunofluorescence staining for the indicated cellular markers (green)
1022 together with HA (magenta). Scale bar: 10 µm.

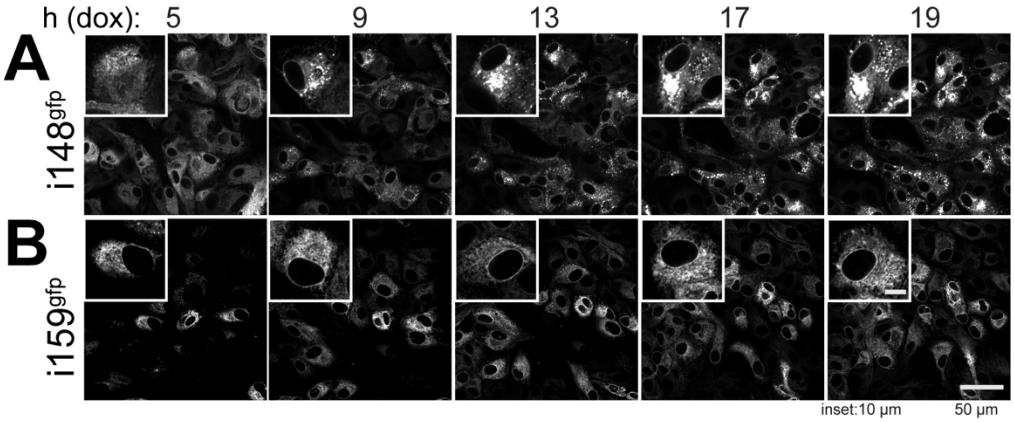

FIG S5. Live-cell Imaging of UL148-GFP and Rh159-GFP during induced ectopic expression. 'Tet-on' ARPE-19 epithelial cells that inducibly express either UL148 or Rh159 fused to green florescent protein (gfp), $i148^{gfp}$ (**A**) and $i159^{gfp}$ (**B**), respectively, were induced for transgene expression using 100 ng/mL doxycycline (dox) and imaged using live-cell microscopy. Images from the selected time points (h post treatment with dox, hpt) are shown. The main scale bar represents 50 µm. For inset panels at upper left of each image, which are magnified 2.4× relative to the main image, the scale bar represents 10 µm. Also see SI Movies S2-S3.

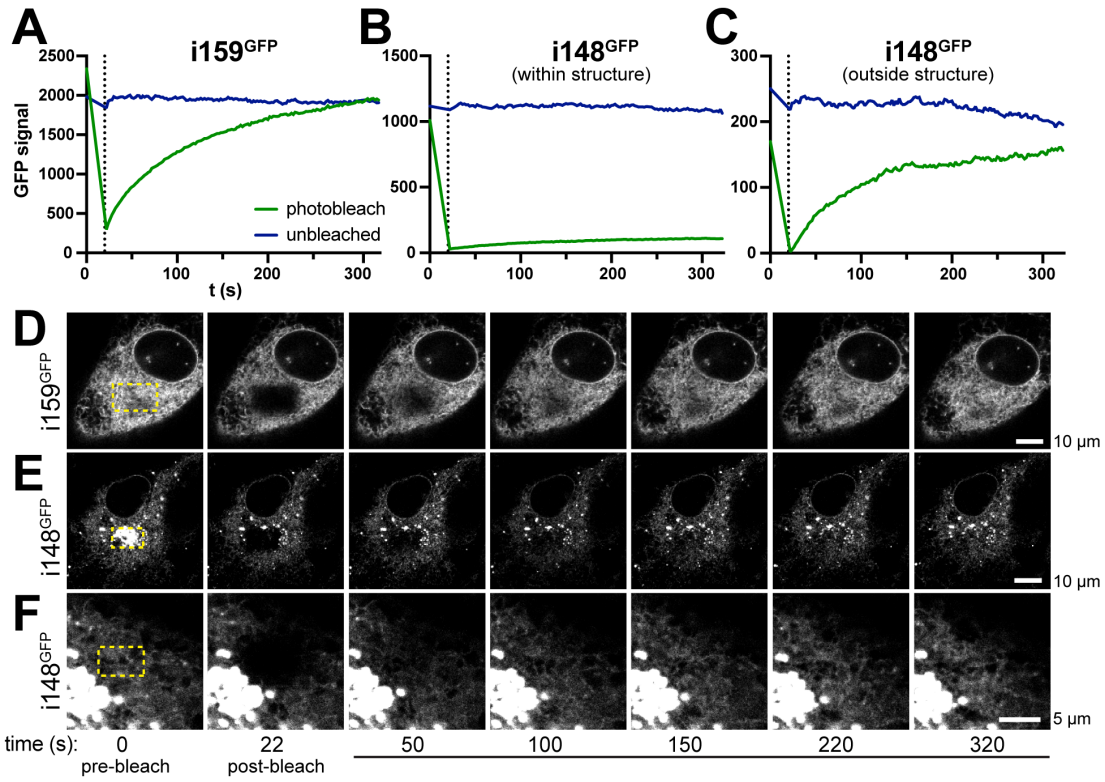

FIG S6. FRAP. ARPE-19 cells that inducibly express Rh159-GFP, i159^{gfp} (**A**) or UL148-GFP, i148^{gfp} (**B-C**) were doxycycline induced for 24 h (100 ng/mL doxycycline (dox). Separate regions of GFP signal in selected cells were photobleached (405 nm laser) or left unbleached, while a third region lacking GFP signal was chosen as a background reference were measured before and during fluorescence recovery after photobleaching (FRAP). Note: background signal was not plotted because values were resolvable from the x-axis. GFP signal intensity is plotted over a time period (seconds, s) starting with an exposure at t=0 (immediately before photobleaching), and including measurements taken every 2 s after photobleaching (0-20 s) until termination of the measurement series at t=322 s (300 s of FRAP). (**D-F**) Images from the selected time points (s, seconds) immediately before and after bleaching, and during fluorescence recovery period. Also see SI Movies S4-S6.

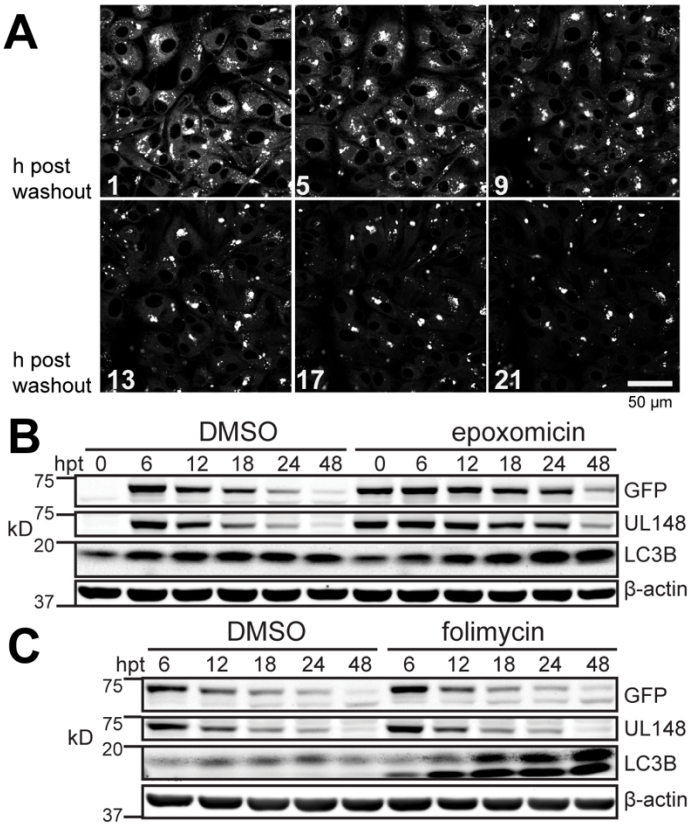

FIG S7: UL148-GFP is stabilized by inhibition of proteasomal but not lysosomal degradation. "Tet-on" ARPE-19 cells that inducibly express UL148-GFP ($i148^{gfp}$) were induced for 24 h by the addition of 100 ng/mL doxycycline (dox), after which the dox inducing agent was washed out and medium containing either the proteasome inhibitor epoxomicin (20 µM) or the proton pump inhibitor folimycin (115 nM) was added and samples were harvested for Western blot analysis at the indicated times post treatment (h post treatment, hpt) with folimycin or epoxomicin. DMSO was added at 0.1% to control for folimycin, or 1% to control for epoxomicin. Also see SI Movie S7.

1058
1059

TABLE S1. Oligonucleotide primers and synthetic DNAs.

Name	Sequence (5' to 3')
148_eGFP_Fw	ACCTGGTGTCGCGGCGTCGGATGGTGAGCAAGGGGGAGGAGCTTTTTACTGGCGTTGTTC
Gibs_eGFP_Rv	CGGCCGCCACTGTGCTGGATTACTTATACAGCTCGTCCATACCCAG
Gib_148_Fw	TGTGGTGGAATTCTGCAGATTGCCACCATGTTGCGCTTGCTG
148_noStopRv	CCGACGCCGCGACACCAGGTAGGTTATC
159_eGFP_Fw	TCTAAAACGCAGTCGTGAAGCTCATATGGTGAGCAAGGGGGAGGA
159_noStop_Rv	ATGAGCTTCACGACTGCGTTTTAGAAGTG
Gibs_159_Fw	TGTGGTGGAATTCTGCAGATTGCCACCATGGCCTACAACAGC
Rh159_Fw	TGTGGTGGAATTCTGCAGATACCATGGCCTACAACAGCTTCCTTCTCAGCTGCCTTACCATCGCAC TTTTACTG
Rh159_HA_Rv	CGGCCGCCACTGTGCTGGATCTATTAGGCGTAGTCTGGGACGTCGTATGGGTAATGAGCTTCACG ACTGCGTTTTAGAAGTG
PpuISceKanGibs_Fw	CATTCACCTGAACCCATAGGTCCTGCCTGGCAGAGAATCTTAGGGATAACAGGGTAATCG
PpuISceKanGibs _Rv	AGATTCTCTGCCAGGCAGGACCTATGGGTTCAGGTGAATGGCCAGTGTTACAACCAATTA
Rh159_Fw_recomb	GGGCGGTGGCCGGCACGCCGCATTTCCTAACCCGCGCAGCATGGCCTACAACAGCTTCCT
Rh159_Rv_recomb	CGCGAACGACGTGTGACGAGGACGTGGTTTCCGCAAGCCTTTAGGCGTAGTCTGGGACG
TB_159HAseq_F	AGTGTTTATGAGTCGGGCGG
TB_159HAseq_R	GTGGCGACGTGGATTTCTTG
EGFP-P2A-3XHA	GTCGACTGGATCCGGTACCGAATTCGCCACCATGGTGAGCAAGGGGGAGGAGCTTTTTACTGGC GTTGTTCCCATCCTGGTTGAGTTGGATGGGGATGTCAACGGCCACAAGTTCAGCGTTTCTGGAGA AGGAGAAGGCGACGCAACCTATGGGAAGCTCACTTTGAAATTCATATGCACCACCGGTAAACTCC CAGTCCCCTGGCCTACCCTGGTCACTACCTTGACATATGGAGTTCAGTGCTTTTCTCGATACCCCG ACCACATGAAGCAGCACGATTTTTTCAAATCTGCAATGCCCGAGGGCTATGTACAAGAGAGGACCA TTTTCTTCAAAGACGACGGCAATTACAAGACCAGGGCCGAGGTCAAATTTGAAGGGGACACTCTTG TGAATCGGATCGAACTTAAAGGGATCGATTTCAAAGAGGACGGAAACATACTGGGGCATAAGCTG GAATACAACTACAATAGCCATAATGTTTACATTATGGCAGACAAGCAGAAAAACGGTATTAAGGTCA ACTTCAAGATACGGCATAACATTGAAGATGGGTCAGTCCAGCTTGCTGACCATTATCAGCAGAATA CACCCATTGGCGATGGTCCCGTGCTTTTGCCTGACAACCACTACCTTTCTACCCAAAGCGCATTGT CAAAAGATCCTAACGAGAAGAGAGATCATATGGTCCTTTTGGAGTTCGTAACCGCAGCTGGTATAA CTCTGGGTATGGACGAGCTGTATAAGGGCTCAGGGGCTACAAATTTTAGTCTCCTTAAACAAGCCG GAGATGTCGAAGAGAACCCTGGGCCTTACCCATATGACGTTCCTGACTATGCCGGTTACCCCTAT GATGTGCCAGATTATGCCGGATCTTATCCTTACGATGTACCTGACTATGCAGGTGGGAGTGGCAT GAATTACGTGGGGCAGC
Gibs_Age_159_Fw	CCGTACCACTTCCTACCCTCGTAAACCGGTGCCACCATGGCCTACAACAG
Gibs_Mlu_GFP_Rv	ACCCGGCGCGGAGGCCAGATCTTAACGCGTTTACTTATACAGCTCGTCCATACC
tRFP linker Fw	CCACTTCCTACCCTCGTAAACCGGTGAATTCGCCACCATGAGCGAGCTGAT
tRFP linker Rv	GCGCGGAGGCCAGATCTTAACGCGTGCGGCCGCTCGAGAATTCATCTGTGCCCCAGTTTGC

1060
1061
1062
1063
1064
1065
1066
1067
1068
1069
1070

1071
1072

TABLE S2. Antibodies Used in Immunofluorescence Microscopy

Primary Antibody	Host species	Isotype	Clone	Vendor	Catalog No.	Dilution used
Calnexin	Mouse	mAb IgG1	37	BD Biosciences	610523	1:50
Calnexin	Rabbit	mAb IgG	C5C9	Cell Signaling Tech.	2679	1:50
Syntaxin 6	Rabbit	mAb IgG	C34B2	Cell Signaling Tech.	2869	1:50
SYVN1 (Hrd1)	Rabbit	mAb IgG	D3O2A	Cell Signaling Tech.	14773	1:500
SEL1L	Rabbit	pAb	n/a	Sigma	S3699	1:50
KDEL	Mouse	IgG2a	10C3	Enzo Life Sci., Inc.	ADI-SPA-827-D	1:50
PDI	Rabbit	mAb IgG	C81H6	Cell Signaling Tech.	3501	1:50
Herp (HerpUD1)	Rabbit	pAb IgG	n/a	Proteintech	10813-1-AP	1:50
VCP	Mouse	IgG2a	5	Invitrogen / Life Technologies	MA3-004	1:50
Calreticulin	Rabbit	mAb IgG	D3E6	Cell Signaling Tech.	12238	1:200
Ribophorin 1 (RPN1)	Rabbit	pAb IgG		ThermoFisher / Invitrogen	PA5-65662	1:50
EDEM-1	Mouse	mAb IgM	D-1	Santa Cruz	sc-377394	1:50
GABARAP	Rabbit	mAb	E1J4E	Cell Signaling Tech.	13733	1:200
LC3B	Rabbit	mAb	D11	Cell Signaling Tech.	3868	1:200
HA epitope	Chicken	IgY		Bethyl	A190-106A	1:200
HCMV glycoprotein H (gH)	Mouse	IgG2b	14-4b	Gift of William J. Britt, M.D.	n/a	1: 50
Reticulon-3 (RTN3)	Mouse	IgG2a		ThermoFisher / Invitrogen	MA5-15538	1: 200
HA epitope	Rabbit	pAb		Bethyl	A190-108A	1:1000
Secondary Antibody	**Host species**	**Isotype**		**Vendor**	**Catalog No.**	**Dilution used**
Alexa Fluor 488 anti-Mouse IgG (H+L), cross adsorbed	Goat	IgG		ThermoFisher / Invitrogen	A11001	1:1000
Alexa Fluor 488 anti-Rabbit IgG (H+L) Cross-Adsorbed	Goat	IgG		ThermoFisher / Invitrogen	A11008	1:1000
Alexa Fluor 594 anti-Rabbit IgG (H+L) Cross-Adsorbed	Goat	IgG		ThermoFisher / Invitrogen	A11012	1:1000
Alexa Fluor 594 anti-Mouse IgG (H+L) Cross-Adsorbed	Goat	IgG		ThermoFisher / Invitrogen	A11005	1:1000
Alexa Fluor 647 anti-Chicken IgY (H+L)	Goat	IgG		ThermoFisher / Invitrogen	A11039	1:1000

1073
1074
1075

1076
1077
1078 **SUPPLEMENTARY VIDEO FILES.**
1079
1080 **Movie S1:** STEM tomography of UL148 ER structures in wildtype HCMV infected fibroblasts at 5
1081 dpi.
1082 **Movie S2:** i148^{gfp} cells from 2-19 h post dox induction.
1083 **Movie S3:** i159^{gfp} cells from 2-19 h post dox induction.
1084 **Movie S4**: FRAP of UL148-GFP signal within ER structure.
1085 **Movie S5:** FRAP of UL148-GFP signal outside ER structure.
1086 **Movie S6:** FRAP of Rh159-GFP signal.
1087 **Movie S7:** i148^{gfp} cells from 30 min to 22 h 07 min post washout of doxycycline (dox).
1088 **Movie S8:** i148^{gfp} cells in the presence of 0.01% DMSO, from 2-19 h post dox induction.
1089 **Movie S9:** i148^{gfp} cells in the presence of 1.1 μM GSK2606414, from 2-19 h post dox induction.
1090 **Movie S10:** i148^{gfp} cells in the presence of 200 nM ISRIB, from 2-19 h post dox induction.
1091
1092
1093
1094

1095 **REFERENCES.**
1096

1097 1. Li G, Nguyen CC, Ryckman BJ, Britt WJ, Kamil JP. 2015. A viral regulator of glycoprotein
1098 complexes contributes to human cytomegalovirus cell tropism. Proc Natl Acad Sci U S A
1099 112:4471-6.
1100 2. Wille PT, Knoche AJ, Nelson JA, Jarvis MA, Johnson DC. 2010. A human cytomegalovirus gO-
1101 null mutant fails to incorporate gH/gL into the virion envelope and is unable to enter
1102 fibroblasts and epithelial and endothelial cells. J Virol 84:2585-96.
1103 3. Jiang XJ, Adler B, Sampaio KL, Digel M, Jahn G, Ettischer N, Stierhof YD, Scrivano L,
1104 Koszinowski U, Mach M, Sinzger C. 2008. UL74 of human cytomegalovirus contributes to
1105 virus release by promoting secondary envelopment of virions. J Virol 82:2802-12.
1106 4. Zhou M, Lanchy JM, Ryckman BJ. 2015. Human Cytomegalovirus gH/gL/gO Promotes the
1107 Fusion Step of Entry into All Cell Types, whereas gH/gL/UL128-131 Broadens Virus Tropism
1108 through a Distinct Mechanism. J Virol 89:8999-9009.
1109 5. Wu Y, Prager A, Boos S, Resch M, Brizic I, Mach M, Wildner S, Scrivano L, Adler B. 2017.
1110 Human cytomegalovirus glycoprotein complex gH/gL/gO uses PDGFR-alpha as a key for
1111 entry. PLoS Pathog 13:e1006281.
1112 6. Kabanova A, Marcandalli J, Zhou T, Bianchi S, Baxa U, Tsybovsky Y, Lilleri D, Silacci-Fregni C,
1113 Foglierini M, Fernandez-Rodriguez BM, Druz A, Zhang B, Geiger R, Pagani M, Sallusto F,
1114 Kwong PD, Corti D, Lanzavecchia A, Perez L. 2016. Platelet-derived growth factor-alpha
1115 receptor is the cellular receptor for human cytomegalovirus gHgLgO trimer. Nat Microbiol
1116 1:16082.
1117 7. Wu K, Oberstein A, Wang W, Shenk T. 2018. Role of PDGF receptor-alpha during human
1118 cytomegalovirus entry into fibroblasts. Proc Natl Acad Sci U S A
1119 doi:10.1073/pnas.1806305115.
1120 8. Nguyen CC, Siddiquey MNA, Zhang H, Li G, Kamil JP. 2018. Human Cytomegalovirus Tropism
1121 Modulator UL148 Interacts with SEL1L, a Cellular Factor That Governs Endoplasmic
1122 Reticulum-Associated Degradation of the Viral Envelope Glycoprotein gO. J Virol 92:e00688-
1123 18.
1124 9. Wang ECY, Pjechova M, Nightingale K, Vlahava VM, Patel M, Ruckova E, Forbes SK, Nobre L,
1125 Antrobus R, Roberts D, Fielding CA, Seirafian S, Davies J, Murrell I, Lau B, Wilkie GS, Suarez
1126 NM, Stanton RJ, Vojtesek B, Davison A, Lehner PJ, Weekes MP, Wilkinson GWG, Tomasec P.
1127 2018. Suppression of costimulation by human cytomegalovirus promotes evasion of cellular
1128 immune defenses. Proc Natl Acad Sci U S A 115:4998-5003.
1129 10. Siddiquey MNA, Zhang H, Nguyen CC, Domma AJ, Kamil JP. 2018. The Human
1130 Cytomegalovirus Endoplasmic Reticulum-Resident Glycoprotein UL148 Activates the
1131 Unfolded Protein Response. J Virol 92:e00896-18.
1132 11. Sinzger C, Hahn G, Digel M, Katona R, Sampaio KL, Messerle M, Hengel H, Koszinowski U,
1133 Brune W, Adler B. 2008. Cloning and sequencing of a highly productive, endotheliotropic
1134 virus strain derived from human cytomegalovirus TB40/E. J Gen Virol 89:359-68.
1135 12. Das S, Vasanji A, Pellett PE. 2007. Three-dimensional structure of the human
1136 cytomegalovirus cytoplasmic virion assembly complex includes a reoriented secretory
1137 apparatus. J Virol 81:11861-9.
1138 13. Sanchez V, Greis KD, Sztul E, Britt WJ. 2000. Accumulation of virion tegument and envelope
1139 proteins in a stable cytoplasmic compartment during human cytomegalovirus replication:
1140 characterization of a potential site of virus assembly. J Virol 74:975-86.

1141 14. Lilley BN, Ploegh HL. 2005. Multiprotein complexes that link dislocation, ubiquitination, and
1142 extraction of misfolded proteins from the endoplasmic reticulum membrane. Proc Natl Acad
1143 Sci U S A 102:14296-301.
1144 15. Kamhi-Nesher S, Shenkman M, Tolchinsky S, Fromm SV, Ehrlich R, Lederkremer GZ. 2001. A
1145 novel quality control compartment derived from the endoplasmic reticulum. Mol Biol Cell
1146 12:1711-23.
1147 16. Leitman J, Shenkman M, Gofman Y, Shtern NO, Ben-Tal N, Hendershot LM, Lederkremer GZ.
1148 2014. Herp coordinates compartmentalization and recruitment of HRD1 and misfolded
1149 proteins for ERAD. Mol Biol Cell 25:1050-60.
1150 17. Houck SA, Ren HY, Madden VJ, Bonner JN, Conlin MP, Janovick JA, Conn PM, Cyr DM. 2014.
1151 Quality control autophagy degrades soluble ERAD-resistant conformers of the misfolded
1152 membrane protein GnRHR. Mol Cell 54:166-179.
1153 18. Sturgill ER, Malouli D, Hansen SG, Burwitz BJ, Seo S, Schneider CL, Womack JL, Verweij MC,
1154 Ventura AB, Bhusari A, Jeffries KM, Legasse AW, Axthelm MK, Hudson AW, Sacha JB, Picker
1155 LJ, Fruh K. 2016. Natural Killer Cell Evasion Is Essential for Infection by Rhesus
1156 Cytomegalovirus. PLoS Pathog 12:e1005868.
1157 19. Chaumorcel M, Souquere S, Pierron G, Codogno P, Esclatine A. 2008. Human
1158 cytomegalovirus controls a new autophagy-dependent cellular antiviral defense
1159 mechanism. Autophagy 4:46-53.
1160 20. Chaumorcel M, Lussignol M, Mouna L, Cavignac Y, Fahie K, Cotte-Laffitte J, Geballe A, Brune
1161 W, Beau I, Codogno P, Esclatine A. 2012. The human cytomegalovirus protein TRS1 inhibits
1162 autophagy via its interaction with Beclin 1. J Virol 86:2571-84.
1163 21. Alwine JC. 2012. The human cytomegalovirus assembly compartment: a masterpiece of viral
1164 manipulation of cellular processes that facilitates assembly and egress. PLoS Pathog
1165 8:e1002878.
1166 22. Das S, Pellett PE. 2011. Spatial relationships between markers for secretory and endosomal
1167 machinery in human cytomegalovirus-infected cells versus those in uninfected cells. J Virol
1168 85:5864-79.
1169 23. Leitman J, Ron E, Ogen-Shtern N, Lederkremer GZ. 2013. Compartmentalization of
1170 endoplasmic reticulum quality control and ER-associated degradation factors. DNA Cell Biol
1171 32:2-7.
1172 24. Cox DW, Billingsley GD, Callahan JW. 1986. Aggregation of plasma Z type alpha 1-antitrypsin
1173 suggests basic defect for the deficiency. FEBS Lett 205:255-60.
1174 25. Le A, Ferrell GA, Dishon DS, Le QQ, Sifers RN. 1992. Soluble aggregates of the human PiZ
1175 alpha 1-antitrypsin variant are degraded within the endoplasmic reticulum by a mechanism
1176 sensitive to inhibitors of protein synthesis. J Biol Chem 267:1072-80.
1177 26. Lomas DA, Evans DL, Finch JT, Carrell RW. 1992. The mechanism of Z alpha 1-antitrypsin
1178 accumulation in the liver. Nature 357:605-7.
1179 27. Ordonez A, Snapp EL, Tan L, Miranda E, Marciniak SJ, Lomas DA. 2013. Endoplasmic
1180 reticulum polymers impair luminal protein mobility and sensitize to cellular stress in alpha1-
1181 antitrypsin deficiency. Hepatology 57:2049-60.
1182 28. Ekeowa UI, Freeke J, Miranda E, Gooptu B, Bush MF, Perez J, Teckman J, Robinson CV,
1183 Lomas DA. 2010. Defining the mechanism of polymerization in the serpinopathies. Proc Natl
1184 Acad Sci U S A 107:17146-51.

1185 29. Suhy DA, Giddings TH, Jr., Kirkegaard K. 2000. Remodeling the endoplasmic reticulum by
1186 poliovirus infection and by individual viral proteins: an autophagy-like origin for virus-
1187 induced vesicles. J Virol 74:8953-65.
1188 30. Windsor M, Hawes P, Monaghan P, Snapp E, Salas ML, Rodriguez JM, Wileman T. 2012.
1189 Mechanism of collapse of endoplasmic reticulum cisternae during African swine fever virus
1190 infection. Traffic 13:30-42.
1191 31. Miller S, Krijnse-Locker J. 2008. Modification of intracellular membrane structures for virus
1192 replication. Nat Rev Microbiol 6:363-74.
1193 32. Siddiquey MNA, Zhang H, Nguyen CC, Domma AJ, Kamil JP. 2018. The human
1194 cytomegalovirus ER resident glycoprotein UL148 activates the unfolded protein response. J
1195 Virol doi:10.1128/JVI.00896-18.
1196 33. Cormack BP, Valdivia RH, Falkow S. 1996. FACS-optimized mutants of the green fluorescent
1197 protein (GFP). Gene 173:33-8.
1198 34. Khaminets A, Heinrich T, Mari M, Grumati P, Huebner AK, Akutsu M, Liebmann L, Stolz A,
1199 Nietzsche S, Koch N, Mauthe M, Katona I, Qualmann B, Weis J, Reggiori F, Kurth I, Hubner
1200 CA, Dikic I. 2015. Regulation of endoplasmic reticulum turnover by selective autophagy.
1201 Nature 522:354-8.
1202 35. Meng L, Mohan R, Kwok BH, Elofsson M, Sin N, Crews CM. 1999. Epoxomicin, a potent and
1203 selective proteasome inhibitor, exhibits in vivo antiinflammatory activity. Proc Natl Acad Sci
1204 U S A 96:10403-8.
1205 36. Muroi M, Shiragami N, Nagao K, Yamasaki M, Takatsuki A. 1993. Folimycin (concanamycin
1206 A), a specific inhibitor of V-ATPase, blocks intracellular translocation of the glycoprotein of
1207 vesicular stomatitis virus before arrival to the Golgi apparatus. Cell Struct Funct 18:139-49.
1208 37. Muroi M, Takasu A, Yamasaki M, Takatsuki A. 1993. Folimycin (concanamycin A), an
1209 inhibitor of V-type H(+)-ATPase, blocks cell-surface expression of virus-envelope
1210 glycoproteins. Biochem Biophys Res Commun 193:999-1005.
1211 38. Kondratyev M, Avezov E, Shenkman M, Groisman B, Lederkremer GZ. 2007. PERK-
1212 dependent compartmentalization of ERAD and unfolded protein response machineries
1213 during ER stress. Exp Cell Res 313:3395-407.
1214 39. Harding HP, Novoa I, Zhang Y, Zeng H, Wek R, Schapira M, Ron D. 2000. Regulated
1215 translation initiation controls stress-induced gene expression in mammalian cells. Mol Cell
1216 6:1099-108.
1217 40. Palam LR, Baird TD, Wek RC. 2011. Phosphorylation of eIF2 facilitates ribosomal bypass of
1218 an inhibitory upstream ORF to enhance CHOP translation. J Biol Chem 286:10939-49.
1219 41. Vattem KM, Wek RC. 2004. Reinitiation involving upstream ORFs regulates ATF4 mRNA
1220 translation in mammalian cells. Proc Natl Acad Sci U S A 101:11269-74.
1221 42. Sidrauski C, Acosta-Alvear D, Khoutorsky A, Vedantham P, Hearn BR, Li H, Gamache K,
1222 Gallagher CM, Ang KK, Wilson C, Okreglak V, Ashkenazi A, Hann B, Nader K, Arkin MR,
1223 Renslo AR, Sonenberg N, Walter P. 2013. Pharmacological brake-release of mRNA
1224 translation enhances cognitive memory. Elife 2:e00498.
1225 43. Sidrauski C, McGeachy AM, Ingolia NT, Walter P. 2015. The small molecule ISRIB reverses
1226 the effects of eIF2alpha phosphorylation on translation and stress granule assembly. Elife 4.
1227 44. Zyryanova AF, Weis F, Faille A, Alard AA, Crespillo-Casado A, Sekine Y, Harding HP, Allen F,
1228 Parts L, Fromont C, Fischer PM, Warren AJ, Ron D. 2018. Binding of ISRIB reveals a
1229 regulatory site in the nucleotide exchange factor eIF2B. Science 359:1533-1536.

1230 45. Sidrauski C, Tsai JC, Kampmann M, Hearn BR, Vedantham P, Jaishankar P, Sokabe M,
1231 Mendez AS, Newton BW, Tang EL, Verschueren E, Johnson JR, Krogan NJ, Fraser CS,
1232 Weissman JS, Renslo AR, Walter P. 2015. Pharmacological dimerization and activation of the
1233 exchange factor eIF2B antagonizes the integrated stress response. Elife 4:e07314.
1234 46. Tsai JC, Miller-Vedam LE, Anand AA, Jaishankar P, Nguyen HC, Renslo AR, Frost A, Walter P.
1235 2018. Structure of the nucleotide exchange factor eIF2B reveals mechanism of memory-
1236 enhancing molecule. Science 359.
1237 47. Gordiyenko Y, Schmidt C, Jennings MD, Matak-Vinkovic D, Pavitt GD, Robinson CV. 2014.
1238 eIF2B is a decameric guanine nucleotide exchange factor with a gamma2epsilon2 tetrameric
1239 core. Nat Commun 5:3902.
1240 48. Harding HP, Zhang Y, Ron D. 1999. Protein translation and folding are coupled by an
1241 endoplasmic-reticulum-resident kinase. Nature 397:271-4.
1242 49. Harding HP, Zhang Y, Bertolotti A, Zeng H, Ron D. 2000. Perk is essential for translational
1243 regulation and cell survival during the unfolded protein response. Mol Cell 5:897-904.
1244 50. Axten JM, Medina JR, Feng Y, Shu A, Romeril SP, Grant SW, Li WH, Heerding DA, Minthorn E,
1245 Mencken T, Atkins C, Liu Q, Rabindran S, Kumar R, Hong X, Goetz A, Stanley T, Taylor JD,
1246 Sigethy SD, Tomberlin GH, Hassell AM, Kahler KM, Shewchuk LM, Gampe RT. 2012.
1247 Discovery of 7-methyl-5-(1-{[3-(trifluoromethyl)phenyl]acetyl}-2,3-dihydro-1H-indol-5-yl)-
1248 7H-p yrrolo[2,3-d]pyrimidin-4-amine (GSK2606414), a potent and selective first-in-class
1249 inhibitor of protein kinase R (PKR)-like endoplasmic reticulum kinase (PERK). J Med Chem
1250 55:7193-207.
1251 51. Tenorio R, Fernandez de Castro I, Knowlton JJ, Zamora PF, Lee CH, Mainou BA, Dermody TS,
1252 Risco C. 2018. Reovirus sigmaNS and muNS Proteins Remodel the Endoplasmic Reticulum to
1253 Build Replication Neo-Organelles. MBio 9.
1254 52. Miller S, Kastner S, Krijnse-Locker J, Buhler S, Bartenschlager R. 2007. The non-structural
1255 protein 4A of dengue virus is an integral membrane protein inducing membrane alterations
1256 in a 2K-regulated manner. J Biol Chem 282:8873-82.
1257 53. Lamond AI, Sleeman JE. 2003. Nuclear substructure and dynamics. Curr Biol 13:R825-8.
1258 54. Granell S, Baldini G, Mohammad S, Nicolin V, Narducci P, Storrie B, Baldini G. 2008.
1259 Sequestration of mutated alpha1-antitrypsin into inclusion bodies is a cell-protective
1260 mechanism to maintain endoplasmic reticulum function. Mol Biol Cell 19:572-86.
1261 55. Lawless MW, Greene CM, Mulgrew A, Taggart CC, O'Neill SJ, McElvaney NG. 2004.
1262 Activation of endoplasmic reticulum-specific stress responses associated with the
1263 conformational disease Z alpha 1-antitrypsin deficiency. J Immunol 172:5722-6.
1264 56. Tirosh B, Iwakoshi NN, Lilley BN, Lee AH, Glimcher LH, Ploegh HL. 2005. Human
1265 cytomegalovirus protein US11 provokes an unfolded protein response that may facilitate
1266 the degradation of class I major histocompatibility complex products. J Virol 79:2768-79.
1267 57. Wiertz EJ, Jones TR, Sun L, Bogyo M, Geuze HJ, Ploegh HL. 1996. The human
1268 cytomegalovirus US11 gene product dislocates MHC class I heavy chains from the
1269 endoplasmic reticulum to the cytosol. Cell 84:769-79.
1270 58. van den Boomen DJ, Timms RT, Grice GL, Stagg HR, Skodt K, Dougan G, Nathan JA, Lehner
1271 PJ. 2014. TMEM129 is a Derlin-1 associated ERAD E3 ligase essential for virus-induced
1272 degradation of MHC-I. Proc Natl Acad Sci U S A 111:11425-30.
1273 59. Caramelo JJ, Parodi AJ. 2008. Getting in and out from calnexin/calreticulin cycles. J Biol
1274 Chem 283:10221-5.

1275 60. Hammond C, Braakman I, Helenius A. 1994. Role of N-linked oligosaccharide recognition,
1276 glucose trimming, and calnexin in glycoprotein folding and quality control. Proc Natl Acad
1277 Sci U S A 91:913-7.
1278 61. Zhou M, Yu Q, Wechsler A, Ryckman BJ. 2013. Comparative analysis of gO isoforms reveals
1279 that strains of human cytomegalovirus differ in the ratio of gH/gL/gO and gH/gL/UL128-131
1280 in the virion envelope. J Virol 87:9680-90.
1281 62. Zhang L, Zhou M, Stanton R, Kamil J, Ryckman BJ. 2018. Expression Levels of Glycoprotein O
1282 (gO) Vary between Strains of Human Cytomegalovirus, Influencing the Assembly of gH/gL
1283 Complexes and Virion Infectivity. J Virol 92.
1284 63. Sifers RN, Brashears-Macatee S, Kidd VJ, Muensch H, Woo SL. 1988. A frameshift mutation
1285 results in a truncated alpha 1-antitrypsin that is retained within the rough endoplasmic
1286 reticulum. J Biol Chem 263:7330-5.
1287 64. Choudhury P, Liu Y, Bick RJ, Sifers RN. 1997. Intracellular association between UDP-
1288 glucose:glycoprotein glucosyltransferase and an incompletely folded variant of alpha1-
1289 antitrypsin. J Biol Chem 272:13446-51.
1290 65. Tsao YS, Ivessa NE, Adesnik M, Sabatini DD, Kreibich G. 1992. Carboxy terminally truncated
1291 forms of ribophorin I are degraded in pre-Golgi compartments by a calcium-dependent
1292 process. J Cell Biol 116:57-67.
1293 66. de Virgilio M, Weninger H, Ivessa NE. 1998. Ubiquitination is required for the retro-
1294 translocation of a short-lived luminal endoplasmic reticulum glycoprotein to the cytosol for
1295 degradation by the proteasome. J Biol Chem 273:9734-43.
1296 67. Johnston JA, Ward CL, Kopito RR. 1998. Aggresomes: a cellular response to misfolded
1297 proteins. J Cell Biol 143:1883-98.
1298 68. Johnston JA, Illing ME, Kopito RR. 2002. Cytoplasmic dynein/dynactin mediates the
1299 assembly of aggresomes. Cell Motil Cytoskeleton 53:26-38.
1300 69. Pankiv S, Alemu EA, Brech A, Bruun JA, Lamark T, Overvatn A, Bjorkoy G, Johansen T. 2010.
1301 FYCO1 is a Rab7 effector that binds to LC3 and PI3P to mediate microtubule plus end-
1302 directed vesicle transport. J Cell Biol 188:253-69.
1303 70. Hummel T, Krukkert K, Roos J, Davis G, Klambt C. 2000. Drosophila Futsch/22C10 is a
1304 MAP1B-like protein required for dendritic and axonal development. Neuron 26:357-70.
1305 71. Wang H, Bedford FK, Brandon NJ, Moss SJ, Olsen RW. 1999. GABA(A)-receptor-associated
1306 protein links GABA(A) receptors and the cytoskeleton. Nature 397:69-72.
1307 72. Zhang K, Daigle JG, Cunningham KM, Coyne AN, Ruan K, Grima JC, Bowen KE, Wadhwa H,
1308 Yang P, Rigo F, Taylor JP, Gitler AD, Rothstein JD, Lloyd TE. 2018. Stress Granule Assembly
1309 Disrupts Nucleocytoplasmic Transport. Cell 173:958-971 e17.
1310 73. Li YR, King OD, Shorter J, Gitler AD. 2013. Stress granules as crucibles of ALS pathogenesis. J
1311 Cell Biol 201:361-72.
1312 74. Hetz C, Saxena S. 2017. ER stress and the unfolded protein response in neurodegeneration.
1313 Nat Rev Neurol 13:477-491.
1314 75. Kirchoff V, Wong S, St JS, Pari GS. 2002. Generation of a life-expanded rhesus monkey
1315 fibroblast cell line for the growth of rhesus rhadinovirus (RRV). Arch Virol 147:321-33.
1316 76. Smith IL, Taskintuna I, Rahhal FM, Powell HC, Ai E, Mueller AJ, Spector SA, Freeman WR.
1317 1998. Clinical failure of CMV retinitis with intravitreal cidofovir is associated with antiviral
1318 resistance. Arch Ophthalmol 116:178-85.

1319 77. Murphy E, Yu D, Grimwood J, Schmutz J, Dickson M, Jarvis MA, Hahn G, Nelson JA, Myers
1320 RM, Shenk TE. 2003. Coding potential of laboratory and clinical strains of human
1321 cytomegalovirus. Proc Natl Acad Sci U S A 100:14976-81.
1322 78. Stanton RJ, Baluchova K, Dargan DJ, Cunningham C, Sheehy O, Seirafian S, McSharry BP,
1323 Neale ML, Davies JA, Tomasec P, Davison AJ, Wilkinson GW. 2010. Reconstruction of the
1324 complete human cytomegalovirus genome in a BAC reveals RL13 to be a potent inhibitor of
1325 replication. J Clin Invest 120:3191-208.
1326 79. Hobom U, Brune W, Messerle M, Hahn G, Koszinowski UH. 2000. Fast screening procedures
1327 for random transposon libraries of cloned herpesvirus genomes: mutational analysis of
1328 human cytomegalovirus envelope glycoprotein genes. J Virol 74:7720-9.
1329 80. Chang WL, Barry PA. 2003. Cloning of the full-length rhesus cytomegalovirus genome as an
1330 infectious and self-excisable bacterial artificial chromosome for analysis of viral
1331 pathogenesis. J Virol 77:5073-83.
1332 81. Tischer BK, Smith GA, Osterrieder N. 2010. En passant mutagenesis: a two step markerless
1333 red recombination system. Methods Mol Biol 634:421-30.
1334 82. Tischer BK, von Einem J, Kaufer B, Osterrieder N. 2006. Two-step red-mediated
1335 recombination for versatile high-efficiency markerless DNA manipulation in Escherichia coli.
1336 Biotechniques 40:191-7.
1337 83. Dietz AN, Villinger C, Becker S, Frick M, von Einem J. 2018. A Tyrosine-Based Trafficking
1338 Motif of the Tegument Protein pUL71 Is Crucial for Human Cytomegalovirus Secondary
1339 Envelopment. J Virol 92.
1340 84. Hohn K, Sailer M, Wang L, Lorenz M, Schneider ME, Walther P. 2011. Preparation of
1341 cryofixed cells for improved 3D ultrastructure with scanning transmission electron
1342 tomography. Histochem Cell Biol 135:1-9.
1343 85. Villinger C, Schauflinger M, Gregorius H, Kranz C, Hohn K, Nafeey S, Walther P. 2014. Three-
1344 dimensional imaging of adherent cells using FIB/SEM and STEM. Methods Mol Biol
1345 1117:617-38.
1346 86. Kremer JR, Mastronarde DN, McIntosh JR. 1996. Computer visualization of three-
1347 dimensional image data using IMOD. J Struct Biol 116:71-6.
1348 87. Britt WJ, Jarvis MA, Drummond DD, Mach M. 2005. Antigenic domain 1 is required for
1349 oligomerization of human cytomegalovirus glycoprotein B. J Virol 79:4066-79.
1350

1351